High-Resolution Airborne Polarimetric Microwave Imaging of Snow Cover During the NASA Cold Land Processes Experiment

Borislava Boba Stankov, Donald W. Cline, Bob L. Weber, Albin J. Gasiewski, *Fellow, IEEE*, and Gary A. Wick

***Abstract*—We present a detailed analysis of the airborne passive microwave remote-sensing data that were collected at a broad range of microwave bands and at a high spatial resolution during the 2002 and 2003 National Aeronautics and Space Administration Cold Land Processes Experiment (CLPX). An accurate measurement of snowpack properties using passive microwave observations requires the detailed knowledge of the relationship between snowpack geophysical parameters and the upwelling polarimetric brightness signature. The principle microwave instrument used for the CLPX was the polarimetric scanning radiometer (PSR), which provided ∼100-m resolution maps of the snow emissivity at all Advanced Microwave Scanning Radiometer for the Earth Observing System (AMSR-E) bands during several intensive observation periods over the Colorado Rocky Mountains. The observed conditions included drought, normal snowpack, and spring snowmelt. The PSR and related ground-based observations of snowpack properties made during the 2002 and 2003 CLPX campaigns provide a comprehensive high-resolution passive microwave data set. Results show that the high-resolution PSR data exhibit emissivity modes that are similar to those observed in the historical data sets, and that the empirical relationships between the emissivity and the snow water equivalent (SWE), after the effects of macrovegetation are removed, closely match those found in the past theoretical studies. The use of the 89-GHz channel in the empirical relationships provides improved accuracy under dry snow conditions and a small SWE; however, the variability of the SWE–emissivity relationships increases with an increasing SWE. A summary of the observed relationships between the emissivity spectra of snow and snowpack properties is presented. Comparison of the total water content from the AMSR-E and PSR observations shows that the satellite measurements underestimated the total volume of water storage from airborne observations on the average by a factor of five.**

***Index Terms*—Airborne polarimetric scanning radiometer (PSR), beam polarization correction, georegistration, microwave emissivity, passive microwave remote sensing, retrieval algorithm development, snowpack, snow water equivalent (SWE), topography, validation.**

Manuscript received September 11, 2007; revised February 21, 2008 and April 21, 2008. Current version published October 1, 2008. While working on this paper, B. B. Stankov was with the Earth Systems research Laboratory, National Oceanic and Atmospheric Administration.

B. B. Stankov is currently with the Cooperative Institute for Research in Environmental Sciences, University of Colorado, Boulder, CO 80305 USA (e-mail: B.Boba.Stankov@noaa.gov).

D. W. Cline is with the National Operational Hydrologic Remote Sensing Center, National Weather Service, National Oceanic and Atmospheric Administration, Chanhassen, MN 55317 USA.

B. L. Weber and A. J. Gasiewski are with the Department of Electrical and Computer Engineering, University of Colorado, Boulder, CO 80309 USA.

G. A. Wick is with the Earth Systems Research Laboratory, National Oceanic and Atmospheric Administration, Boulder, CO 80305 USA.

Color versions of one or more of the figures in this paper are available online at http://ieeexplore.ieee.org.

Digital Object Identifier 10.1109/TGRS.2008.2000625

NOMENCLATURE

AGL	Above ground level.
AMSR-E	Advanced Microwave Scanning Radiometer for the Earth Observing System.
CLPX	Cold Land Processes Experiment.
HUT	Helsinki University of Technology.
ISA	Intensive study area.
ISFF	Integrated Surface Flux Facility.
LAPS	Local Analysis and Prediction System.
MRT	Microwave radiative transfer.
MSA	Mesocell study area.
NARR	North American Regional Reanalysis.
NCAR	National Center for Atmospheric Research.
NCEP	National Centers for Environmental Prediction.
NOAA	National Oceanic and Atmospheric Administration.
NOHRSC	National Operational Hydrologic Remote Sensing Center.
NSIDC	National Snow and Ice Data Center.
NWS	National Weather Service.
PSR	Polarimetric scanning radiometer.
RFI	Radio-frequency interference.
SMMR	Scanning Multichannel Microwave Radiometer.
SWE	Snow water equivalent.
T_B	Brightness temperature.

I. INTRODUCTION

COLD LAND regions play a critical role in the Earth's hydrologic cycle and have a significant impact on global weather and climate through their modulation of the Earth's radiation budget, storage of greenhouse gases in frozen tundra, and moderation of boundary layer fluxes. Furthermore, they are believed to have major secondary impacts on weather and climate through their influence on biota and biogenic processes, and provide an important store of freshwater for human activity. The National Aeronautics and Space Administration (NASA) CLPX was conducted during February 2002, February 2003, and March 2003 to develop the quantitative understanding, models, and measurement techniques that are necessary to extend the local-scale knowledge of cryospheric water fluxes, storage, and transformations to regional and global scales. The goals of the CLPX were to understand the formation and the evolution of snow and to better observe transitions between snow and water in cold regions [1]. The experiment was

sponsored by the NASA Terrestrial Hydrology and the Earth Observing System Programs.

Of particular importance during the CLPX was the identification of optimal means for remotely sensing global properties of the terrestrial cryosphere in preparation for the NASA Cold Lands Pathfinder space experiment [2].[1] One specific goal was the evaluation and the improvement of algorithms to better exploit the snow information contained in polarimetric microwave emission spectra from snow in its various forms. As previously shown [3], useful direct relationships exist between snow-cover parameters and microwave surface emissivity since snow crystals are efficient scatterers of microwave radiation. However, the estimation of snowpack geophysical properties using passive microwave data is made difficult by the dynamic nature of the snowpack and its emission properties, along with its spatial heterogeneity. Accordingly, CLPX goals included a detailed study of the relationship between the microwave emissivity of snow and the snowpack properties on a variety of scales and during several stages of snowpack evolution.

To obtain the necessary microwave data at a high spatial resolution, the NOAA PSR[2] instrument was operated from two different NASA aircraft during intensive observing periods in 2002 and 2003. We present here a summary of the PSR imaging activities during these CLPX phases and use the PSR data set to examine the response to snow cover of the AMSR-E 6.9-, 10.7-, 18.7-, 21.5-, 37-, and 89-GHz bands. The PSR microwave data processing steps are described, and the complete set of the microwave images is presented. Ground-based data are used to develop and verify PSR retrieval algorithms for the SWE. We compare these empirical estimates of the SWE with the results from applying the well-known Chang algorithm [3] to the PSR data. We also compare our empirical estimates to the SWE computed from AMSR-E data and to the SWE measured by NOAA's NOHRSC using gamma radiation spectroscopy.

II. Measurements

A. Site Description

The CLPX study area was located in the northern Colorado Rocky Mountains and focused on three MSAs that included detailed ground-based snowpack measurements. The three 25-km^2 MSAs [1], [4], designated as North Park, Rabbit Ears, and Fraser, were each imaged using seven east–west flight lines [Fig. 1(a), thick red lines]. Each MSA contained three ISAs of 1-km^2 size.

Topography, snow cover, and snow characteristics at the three MSAs represent four of the major global snow-cover classes [1] that, together, comprise 88% of the seasonally snow-covered area of the Earth. Each MSA also represents a distinct cold region physiographic regime, as shown by the 30-m spatial-resolution 21-class land-cover classification scheme [5] of the National Land Cover Data Set for the North Park, Rabbit Ears, and Fraser MSAs [Fig. 1(b)–(d)]. The North Park MSA is generally covered with shallow windswept snow over frozen soil and consists of grassland and shrubs with few trees in the wetter areas. The Rabbit Ears MSA is normally covered with moderate-to-deep snow, and the land cover consists of mixed coniferous and deciduous forest and large forest gaps covered with grass. The Fraser MSA is also normally covered with moderate-to-deep snow with the land cover consisting of coniferous forest at middle and upper elevations and alpine tundra at the highest elevations with irrigated grazing land at the lower elevations. The PSR-imaged areas are slightly larger than the formally designated MSAs, so that the land cover of each extended area contained mixed, coniferous, and deciduous forest in addition to the above-described MSA land cover.

PSR data were collected during three intensive observing periods in February 2002 (wintertime drought conditions), February 2003 (normal midwinter snow conditions that were generally frozen and dry), and March 2003 (an early spring transitional period when both frozen and thawed, and dry and wet conditions were widespread).

B. PSR

The PSR is the first operational airborne conically scanning radiometer [6] and has been used in several major field experiments to observe microwave emission from soil, oceans, and precipitation, including the SMEX and AMSRIce series, [7], [8]. The PSR concept is based on a set of polarimetric microwave radiometers that are housed inside a sealed scanning drum along with a 10.6-μm wavelength *IR* sensor. The drum protrudes from the bottom of the aircraft fuselage and is supported from the aircraft using a two-axis gimbal mount. The gimbal mount permits the drum to be independently scanned in both azimuth and elevation, thus facilitating a variety of scan modes, including conical, cross-track, along-track, spotlight, and stare modes. Slip rings convey digitized radiometer data streams to the aircraft for archival, processing, and display.

PSR radiometers (Table I) use dual orthogonal linearly polarized lens-feedhorn antennas of high main-beam efficiency ($> 97\%$). Specific steps in the calibration and the processing of the PSR data are discussed in Section III-A. A description of the basic PSR calibration technique has been provided elsewhere [9].

Table II lists the PSR configurations used for the CLPX campaigns and the specifics of each campaign. The instrument was operated in conically scanned mode at an incidence angle of 55° from nadir. During February 2002 and February 2003, the PSR/A scanhead was operated aboard the NASA DC-8 and NASA P-3B, respectively, and during March 2003, the simultaneous operation of two scanheads (PSR/A and PSR/CX) aboard the NASA P-3B provided full polarimetric and spectral simulation of AMSR-E. During the entire experiment, a total of 154 lines was flown over the three MSAs, providing 29 h and 38 min of observation time at the nominal flight altitude of ~2300 m AGL. Flight lines overlapped by ~20% between adjacent PSR swaths.

[1]Renamed the Snow and Cold Land Processes mission per completion of the Decadal Survey (2007) by the U.S. National Research Council.

[2]Now part of the University of Colorado's Center for Environmental Technology; see http://cet.colorado.edu.

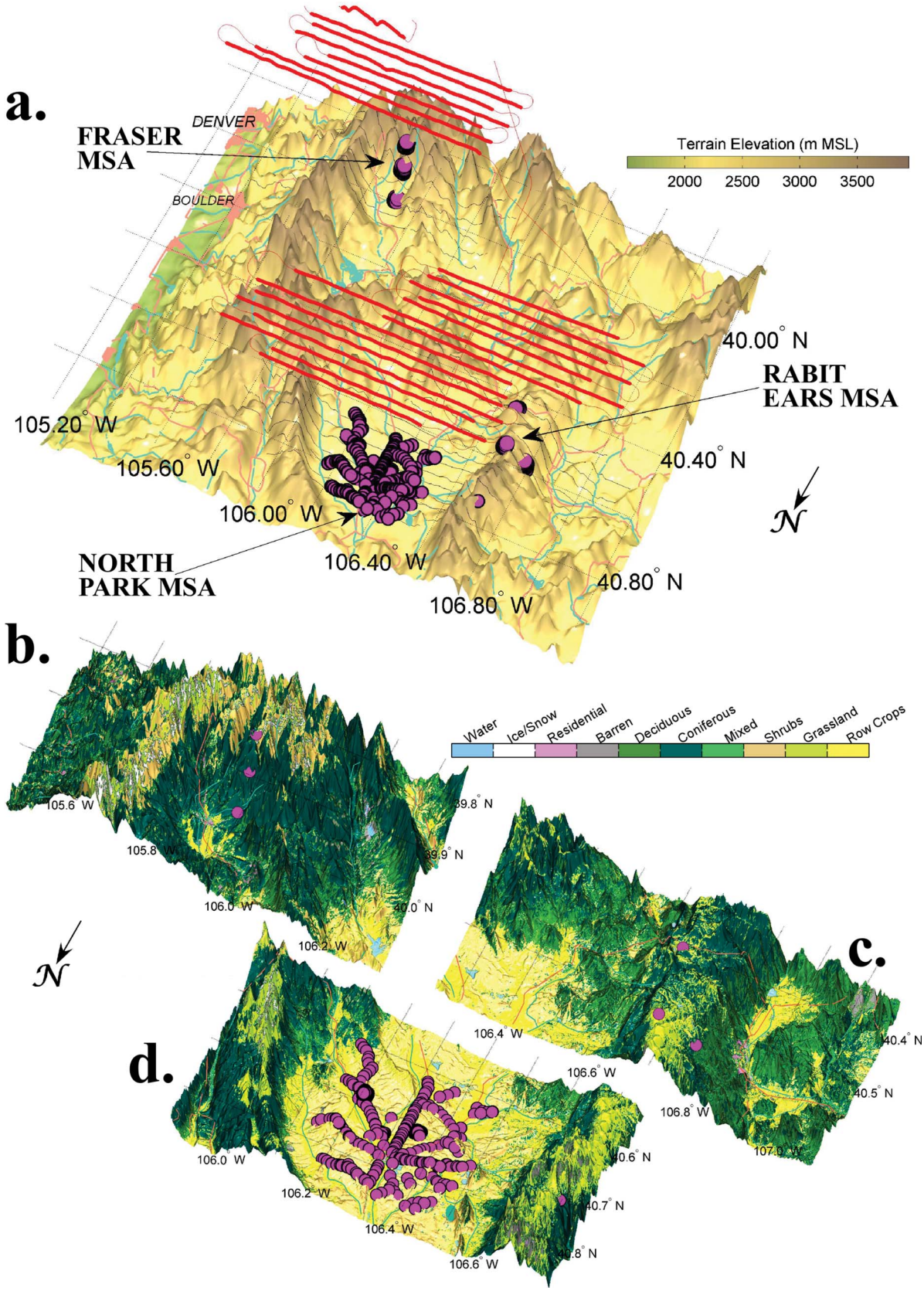

Fig. 1. (a) Three-dimensional rendering of the CLPX Fraser, Rabbit Ears, and North Park MSAs. (Thin red lines) Aircraft flight path on 31 March 2003. (Thin black lines) Flight line projection onto the Earth surface. (Thick red lines) Flight tracks with the PSR in the conical scanning mode. (Magenta circles) ISA snow-pit and (at North Park) extended snow-pit locations. National Land Cover Data 21-class 30-m spatial resolution land cover data from the Landsat Thematic Mapper satellite for (b) Fraser, (c) Rabbit Ears, and (d) North Park. The color scale reflects only the region-relevant land cover out of the 21 classes. Magenta dots show the locations of the ground-based snow-pit SWE measurements. Note the $\sim 154^\circ$ azimuth rotation is used to show ground-based locations that are facing north.

TABLE I
PSR BANDS, POLARIZATIONS, AND 3-dB ANTENNA BEAMWIDTHS FOR CLPX. THE MULTIPLE SUBBAND CHANNELS ON THE PSR/CX ARE USED FOR INTERFERENCE MITIGATION

Scanhead	Band Name	Band (GHz)	Polarizations	Beamwidths
PSR/CX	C	5.8-7.3 (four subbands)	v,h	10°
	X	10.6-10.8 (four subbands)	v,h	6.5°
PSR/A	X	10.6-10.8	v,h	8°
	Ku	18.6-18.8	v,h	8°
	K	21.4-21.7 (H_2O wing)	v,h	8°
	Ka	36-38	v,h	2.3°
	W	86-92	v,h	2.3°
		9.6-11.5 μm IR	Unpolarized	7°

TABLE II
CATALOG OF PSR OBSERVATIONS OVER MSAS DURING THREE CLPX FIELD CAMPAIGNS. MSAS ARE NORTH PARK (NP), RABBIT EARS (RE), AND FRASER MEADOWS (F)

Experiment & Configuration	Date	Obs. Times (UTC)	MSA(s) Imaged	# Flt. Lines	Nominal Flt. Alt. (km AGL)	3 dB Spatial Resolution Range (m) @ 37, 89 GHz	3 dB Spatial Resolution Range (m) @ 10, 18, 21 GHz
CLPX02 PSR/A on NASA DC-8	2/19/02	21:18 - 22:35	RE	7	2.34	88 – 209	308 – 728
	2/21/02	16:45 - 18:49	NP, RE, F	11	2.10	65 – 234	191 – 812
	2/23/02	16:57 - 18:34	NP, RE, F	11	2.10	65 – 203	184 – 708
CLPX03A PSR/A on NASA P-3B	2/22/03	18:35 - 20:35	NP	7	3.93	184 – 334	642 – 1161
	2/23/03	17:35 - 21:37	NP, RE, F	21	2.18	65 – 215	229 – 749
	2/24/03	20:30 - 23:05	NP, RE	14	2.22	71 – 206	246 – 718
	2/25/03	17:30 - 21:00	NP, RE, F	21	2.18	65 – 215	229 – 749
CLPX03B PSR/A & PSR/CX on NASA P-3B	3/25/03	17:50 - 22:05	NP, RE, F	21	2.18	65 – 215	229 – 749
	3/30/03	18:10 - 22:30	NP, RE, F	21	2.18	65 – 215	229 – 749
	3/31/03	17:50 - 21:50	NP, RE, F	21	2.18	65 – 215	229 – 749
Total		29 hr 38 min		154		80 – 226	272 – 787

C. Ground Data Collection

During each aircraft sortie, high-quality spatially intensive *in situ* measurements of snowpack parameters were obtained to support the development and the validation of a passive microwave SWE retrieval algorithm [10]. Each of the nine 1-km^2 ISAs was sectioned into 100×100 m grid cells, each containing snow depth measurement transects, providing 100 measurements of average snow depth for each ISA [11]. In addition, each ISA was divided into 16 250×250 m grid cells containing snow pit (Fig. 1 magenta circles) measurements of the snow depth, the surface wetness, the snow temperature, the soil temperature, the canopy cover, the snow grain size, and the SWE [12]. At the North Park MSA, additional snow-pit measurements were made over a 625-km^2 area. Because the depth transects did not include the measurements of the SWE and the grain size, we computed the SWE at the depth transect locations from the snow depth measurement and the mean snow density from the nearest snow pit [10]. This procedure assumes a little variation in snow density over short distances, which is generally acceptable. We also assigned the grain size measurement at each nearest snow pit to the depth transect location to increase the number of PSR *in situ* comparison points.

D. NWS Gamma SWE System

The NWS NOHRSC provides nationwide operational SWE measurements using a gamma radiation spectrometer that measures upwelling terrestrial gamma radiation intensity. Attenuation of the natural terrestrial gamma radiation by water in the snow together with background gamma radiation measurements that are collected prior to seasonal snowfall is the basis for these SWE estimates [4].

During CLPX observing periods, the NOHRSC's gamma spectrometer was flown aboard the NOAA AC690A aircraft at 150 m AGL along flight lines of variable length within each MSA. These data provided estimates of the average SWE within each of the MSAs [13].

E. LAPS 10-km Surface Temperature

NOAA's LAPS integrates numerous observed meteorological data sets into a collection of atmospheric analyses. LAPS has both analysis and prediction components that provide spatially and temporally continuous atmospheric and land-based fields on a 1040×1240 km grid with a 10-km spatial resolution over Colorado and parts of surrounding states at an hourly temporal resolution [14].

Outputs from the LAPS system include hourly 3-D and surface distributions of atmospheric fields. In this study, we use ground temperature fields in an MRT model to obtain surface emissivity estimates from the measured PSR brightness temperatures T_B.

III. DATA PROCESSING

Primary PSR data processing occurs in multiple stages. After primary radiometric processing was completed, the data processing specific to the CLPX experiment, i.e., georegistration with respect to the CLPX MSA terrain and reorientation

of the PSR polarization basis with regard to the terrain facet normal vectors, was performed.

A. PSR Primary Radiometric Processing

During the operation, several PSR data streams are asynchronously collected, including radiometric voltage, navigation, temperature, scanhead position, and aircraft attitude streams. These data streams are quality checked, interpolated, and calibrated into brightness temperatures [9], [15]. Data collected during wide turns, altitude changes, or any other sudden aircraft movements were discarded. Thus, brightness temperature data that are used for further processing consisted only of cases when: 1) the aircraft was flying over MSAs in straight lines [thick red lines in Fig. 1(a)] with the PSR scanheads operating in the conical mode; 2) the aircraft was flying in a constant angle turn with the scanhead operating in the cross-track mode; and 3) during the steep cold-sky calibration rolls.

During normal scanning operation, but when the aircraft was maneuvering between observation lines, the PSR is operated to periodically observe the external hot and ambient thermal references. One reference is maintained at a constant thermometric temperature of $\sim$65 °C and the other one at the local ambient temperature. Both temperatures are measured and recorded to ± 0.1 °C precision. The hot and ambient loads are observed at $\sim$5-s time intervals, which is a short period compared to the several-minutes thermal time constant of the targets. External hot and ambient blackbody targets are viewed at the beginning and at the end of each flight line over $\sim$5- to 7-min intervals. For times between the hot/ambient calibration looks, the gain and the offset are interpolated. Calibration using thermally stabilized noise diodes within each radiometer is observed every ~ 100 ms to track the short-term gain and the offset fluctuations [9]. The process consists of periodically switching the radiometer inputs to view noise diodes that are attenuated to two distinct temperatures, thus allowing calibration at a high rate without physical motion while using the external calibration targets to provide absolute calibration of the noise diode temperatures. Precision cold sky reference data were provided by rolling the aircraft and the sensor to view 35° above the horizon three times per flight. The cold sky data were used to adjust the external target emission temperatures for residual spillover, reflectivity, and calibration target thermal gradients. The resulting absolute accuracy is estimated to be nominally ± 1 K for the range of brightness temperature T_B values encountered during the CLPX.

B. Georegistration

The primary PSR processing provided brightness temperatures sampled on a conically scanned azimuthal grid. However, the mean terrain elevation and the terrain elevation range for the North Park, Rabbit Ears, and Fraser MSAs are 2727 m (1534-m range), 2584 m (1628-m range), and 2951 m (1810-m range), respectively. For such mountainous terrain with rugged topography, a geolocation procedure based on ray tracing was necessary. U.S. Geological Survey (USGS) terrain elevation data with a 30-m resolution were used to determine the latitude and the longitude of the closest ground facet intersecting the line of sight of a PSR beam. This procedure provided the latitude, the longitude, the terrain elevation, the vector normal of the terrain facet, and the major and minor diameters of the field-of-view ellipse at each measurement point. Variations in the surface elevation resulted in 3-dB spatial resolutions ranging from $\sim$80 to $\sim$790 m, depending on the particular PSR band (Table II) and footprint location.

IV. Radiative Transfer Surface Emissivity Estimate

The PSR brightness temperature T_B at the aircraft altitude consists of contributions from the downwelling radiation reflected at the surface T_R, radiation due to upwelling emission from the atmospheric layers T_U, and radiation due to surface emission T_E [16], i.e.,

$$T_B = T_R + T_U + T_E. \tag{1}$$

Radiation due to reflection at the surface can be expressed in terms of the downwelling radiation at surface T_D and surface emissivity ε_S as

$$T_R = T_D(1 - \varepsilon_S)e^{-\tau \sec\theta} \tag{2}$$

where τ is the optical depth from the surface to the observation altitude H, and θ is the incidence angle. The radiation emitted by the surface can be expressed in terms of surface temperature T_S and surface emissivity as follows:

$$T_E = \varepsilon_S T_S e^{-\tau \sec\theta}. \tag{3}$$

Accordingly

$$T_B = T_D(1 - \varepsilon_S)e^{-\tau \sec\theta} + T_U + \varepsilon_S T_S e^{-\tau \sec\theta}. \tag{4}$$

Solving for the surface emissivity, we have

$$\varepsilon_S = \frac{(T_B - T_U)e^{\tau \sec\theta} - T_D}{(T_S - T_D)}. \tag{5}$$

Equation (5) holds for both horizontal and vertical polarizations. Therefore, if the surface temperature, the downwelling radiation at the surface, and the upwelling radiation at the aircraft altitude are known, we can obtain the surface emissivity from PSR measurements T_B.

A. Surface Emissivity Computation

In (5), T_U, T_D, τ, and T_S are the quantities that need to be obtained from ancillary data. We used the NWS 6-s vertical resolution radiosonde measurements of the atmospheric temperature and humidity profiles in the NOAA/Physical Sciences Division (PSD) [17] MRT model to compute T_U, T_D, and τ for all the cases shown in Table II. This computation assumed the absence of the scattering hydrometeors within the atmosphere. This assumption held for channels 6.9–37 GHz and for all CLPX conditions. However, as shown in Section VII-A, the 89-GHz channel is sensitive to precipitation, and emissivity differences of 13% on consecutive days during February 2003 were observed. Because there were no radiosonde releases

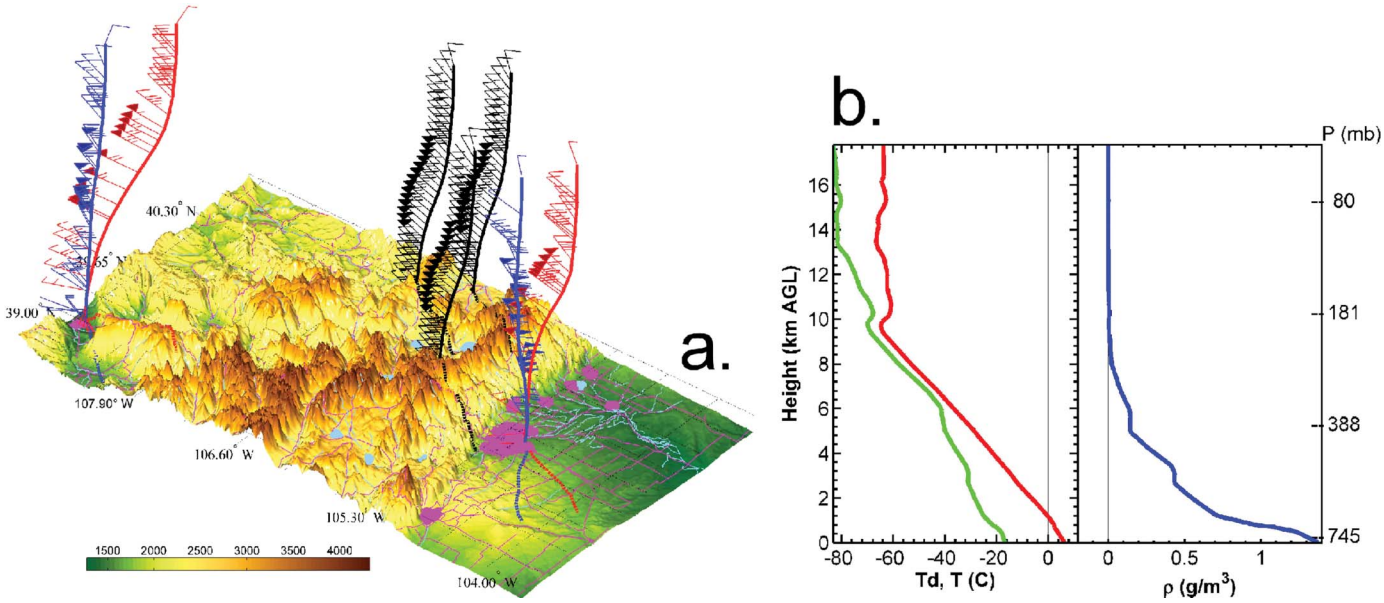

Fig. 2. Example of the radiosonde data used in the surface emissivity calculations in the absence of the local temperature and humidity profile measurements. (a) Three-dimensional aerial view of the two Grand Junction and Denver 6-s NWS radiosonde paths and the terrain-adjusted average profile assigned to the MSAs. (b) Average (red) temperature, (green) dew point, and (blue) absolute humidity profiles.

within the CLPX area during the experiment, the routine 12-hourly NWS radiosonde data ~300 km away from the CLPX domain either in the windward or the lee side of the mountains were used to construct the necessary profiles of temperature and humidity. Fig. 2(a) shows an example of the use of four distant but closest NWS soundings for the 23 February 2002 case to construct temperature and humidity profiles for the atmosphere above the MSAs. Twice-daily NWS soundings are obtained at Grand Junction and Denver, but not in the MSA. However, micrometeorological flux tower measurements of surface pressure and temperature at the North Park MSA were provided by the ISFF of the Earth Observing Laboratory at the NCAR. We averaged the four NWS radiosonde soundings and applied the tower measurements of surface pressure and temperature to the mean profiles. Fig. 2(b) shows the average temperature, the dew-point temperature, and the absolute humidity profiles applied to the MSAs and used in the MRT computation for this case.

To obtain surface temperature data, we used the PSR *IR* sensor and the LAPS ground temperature interpolated to the PSR measurement locations. By always selecting the higher of the two values, we accounted for undercast cases; that is, during clear conditions, the *IR* brightness temperature is very close to the surface temperature, but during cloudy cases, *IR* observations are representative of the highest cloud deck, and the interpolated LAPS ground temperature was used. The difference of the mean MSA *IR* temperature and the mean MSA LAPS ground temperature for all the available clear air cases was computed to be 0.9 K, which would result in the emissivity error of 0.003.

B. Beam Polarization Correction

The horizontal and vertical polarization surface emissivities obtained from (5) are georegistered to the latitude and the longitude of the point where the radiation beam first intercepts the terrain, but then need to be rotated so that they lie in the parallel and perpendicular directions of each terrain facet. Section III-B described the use of the 30-m resolution USGS terrain elevation data to fit a plane to the terrain facet and obtain the vector normal to the terrain facet in addition to obtaining georegistered latitude and longitude. The rotation of the horizontal and vertical polarization emissivities is then accomplished by using the following relationships:

$$\begin{aligned} \varepsilon'_{Sh} &= \varepsilon_{Sv} \sin^2 \alpha + \varepsilon_{Sh} \cos^2 \alpha \\ \varepsilon'_{Sv} &= \varepsilon_{Sv} \cos^2 \alpha + \varepsilon_{Sh} \sin^2 \alpha \end{aligned} \tag{6}$$

where ε_{Sh} and ε_{Sv} are the MRT-computed horizontal and vertical polarization emissivities using (5). The rotation angle between the PSR polarization basis and the natural basis of the terrain facet α is given by (7), shown at the bottom of the page, where the subscripts P and T refer to PSR angles and terrain facet angles, respectively, measured with respect to the Earth. The true azimuth angle is φ, and the true elevation angle is θ. Equations (6) and (7) provide normalized horizontal and vertical polarization surface emissivity images in the instrument angular coordinate system.

V. Mapping and Gridding

The purpose of the surface emissivity mapping and gridding was to accurately geolocate the emissivity field obtained from

$$\tan \alpha = \frac{\cos \varphi_P \sin \theta_T \sin \varphi_T - \sin \varphi_P \sin \theta_T \cos \varphi_T}{\cos \theta_P \sin \varphi_P \sin \theta_T \sin \varphi_T + \cos \theta_P \cos \varphi_P \sin \theta_T \cos \varphi_T + \sin \theta_P \cos \theta_T} \tag{7}$$

the PSR measurements onto a geographic grid for further analysis. To this end, we tested two different gridding algorithms. In the first one, the sampling of the PSR was assumed to be uniform throughout the PSR footprint, and the estimated emissivities were directly applied to every grid cell contained within footprint, with averaging for sampling of a grid cell by multiple footprints. The second algorithm recognizes that the true sampling of the PSR is not uniform and is, instead, more heavily weighted to the center of the footprint. This effect was accounted for by assuming the beam weighting to be given by a $sinc^2$ function. In this approach, for every geographic grid cell, the relative contribution of each radiometric emissivity to the grid value is weighted by the value of the $sinc^2$ function at the corresponding effective radius. Applying the two approaches to a given test case revealed that the second approach took several hours more computing time than the first approach but resulted in little difference in the gridded product. Considering this result and the large volume of PSR data, the first approach was chosen for further analysis in the interest of efficiency. We expect that the second approach may be important in transition areas between forest and open clearings, particularly for the high-frequency channels, but this is left for future study.

The selected gridding algorithm used the size and the location of the radiometric footprint (Section III-B) and a 100-m-resolution grid to determine which grid cell contains data from different sensor footprints. The 100-m resolution was chosen for consistency with the resolution of the highest resolution PSR channels (Table II). For cases where multiple sensor footprints overlapped, the algorithm averaged the data from each individual footprint to estimate the emissivity for each grid cell. The radiometer data were prefiltered in the instrument azimuthal coordinate system prior to gridding. Prefiltering included trend removal and the removal of data spikes. Small brightness offsets between adjacent gridded lines due to calibration drift were removed using the data from the line overlap area ($\sim$20% of the swath width). For grid cells with no corresponding radiometric footprints, the algorithm interpolated the data using a weighted sphere-of-influence technique wherein weighting is based on the inverse of the distance of valid data from the point being interpolated. Extrapolation outside the limits of the flight segment was not permitted. Thus, interpolation over small calibration gaps occurred; however, interpolation over larger gaps was precluded, and the data displayed contain gaps.

The gridded 100-m-resolution PSR microwave data set was used to estimate both brightness temperature and emissivity at the locations of the ground-based *in situ* observations of the SWE [10]. Altogether, during the PSR flights, there were 2707 *in situ* data points, including 2107 from depth transects and 600 from snow-pit observations. North Park contributed 1281 collocated points, Rabbit Ears contributed 1001, and Fraser contributed 425. Of these, 403 were rejected as spurious or, otherwise, out of bounds, resulting in a final data set with 2304 points available for comparison. An Excel table containing 170 columns of ground-based data, collocated PSR data, and HUT model [18] results was archived with the NSIDC for unlimited access to all scientists. PSR-gridded brightness temperature and emissivity data were also archived at the NSIDC for general use.

VI. Weather Conditions

Although snow conditions were originally anticipated to be similar during the same month and for the same area in CLPX02 and CLPX03A, the two seasons exhibited markedly different weather and snowfall amounts. February 2002 was characterized by a high surface pressure system located over the Rocky Mountains that maintained clear air over the three MSAs. In contrast, during February 2003, a stationary cold front meandered from northwest Idaho through northeast Wyoming, northeast Colorado, and to the Oklahoma panhandle, leaving very cold air behind it. Simultaneously, a high surface pressure system over the Canadian border moved into South Dakota on the 24th when the surface low-pressure system was located roughly south of the Colorado Rocky Mountains. This combination of a high-pressure system to the north and a low-pressure system to the south produced upslope air motion in the CLPX area and brought in moist air from the Gulf of Mexico, resulting in precipitation in the mountains with scattered snow showers and overcast conditions.

During the later period of 16–20 March 2003, an extreme snowfall event with up to 2.2-m accumulation occurred over the southern Rocky Mountains and the High Plains region. It is believed that such an event occurs only once per 100 years [19]. This storm was characterized by extraordinary microscale snowfall variability and left significant precipitation over the Fraser MSA. However, by 25 March, a weak high-pressure center situated over Utah–Wyoming border provided clear conditions over the CLPX area. On 28 March, a weak upslope flow provided more light precipitation, but by the flights on 30 and 31 March, the surface high-pressure system centered over southern Utah and the Colorado region provided clear-sky conditions again.

Fig. 3(a) shows a matrix of the three-hourly composite maps of the surface air temperature over Colorado at 2-m height AGL, and Fig. 3(b) shows a matrix of the surface three-hourly accumulated precipitation provided by the 32-km-resolution NOAA NWS NCEP NARR model [20]. The three rows of each map matrix represent the February 2002, February 2003, and March 2003 experiments, and the columns represent individual flight days. As discussed, February 2002 was a dry month with no accumulated precipitation in the 3 h prior to the flights and with the 2-m AGL air temperature varying from -7 °C to 5 °C. The influence of the meandering stationary cold front in February 2003 is shown by the temperatures ranging from -14 °C to -2 °C and the three-hourly accumulated precipitation reaching 6 mm on 22 February, with no precipitation on the 23rd, and then followed by 2 days with lighter precipitation. On 25 and 30 March 2003, general warming in Colorado was observed, but on 31 March, a nearly 10-°C jump in the temperature from the day before was observed. During March 2003, no significant precipitation accumulation was present, although 30 March was hazy, with $\sim$1-mm precipitation observed during the 3 h.

The Pennsylvania State University and NCAR 4500-m-resolution mesoscale model (known as MM5V3) [21] was

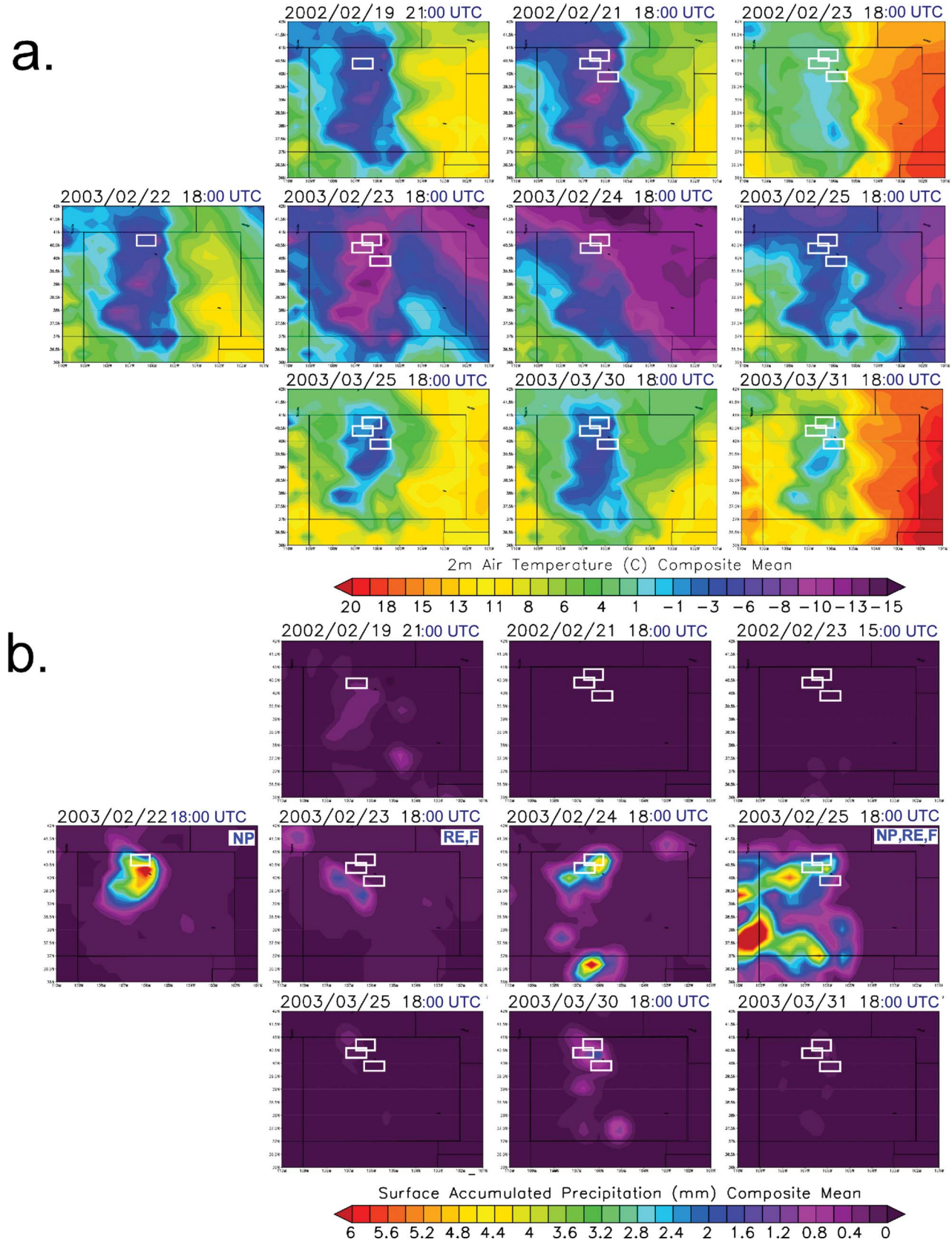

Fig. 3. NOAA NWS NCEP three-hourly NARR composites of (a) surface air temperature (in degrees Celsius) at 2 m AGL and (b) three-hourly surface accumulated precipitation (in millimeters) for all the PSR flight days during CLPX. White squares represent the North Park, Rabbit Ears, and Fraser MSAs observed on that day. Blue codes within the precipitation maps on the February 2003 flights indicate the days when the MM5 model showed precipitation present at each MSA during the flight. NP: North Park. RE: Rabbit Ears. F: Fraser. The date and the observation time are printed above each frame.

run for February and March 2003 CLPX experimental areas. We used these high-resolution MM5 model runs to assess if precipitation was present in the atmosphere during the PSR individual flights. Over the North Park MSA, MM5 shows heavy precipitation on 22 February 2003, no precipitation on 23 February, and light and moderate precipitation on 24 and 25 February 2003, respectively [Fig. 3(b)]. During March 2003, MM5 showed no precipitation on any flight day. Over the Rabbit Ears MSA, MM5 shows moderate precipitation on 23 February 2003, heavy precipitation on 25 February 2003, and no precipitation on any other experimental day. For the Fraser MSA, MM5 shows light precipitation on 23 February 2003, moderate precipitation on 25 February, and no precipitation on any other flight day.

GOES-8 11-μm *IR* window channel images and NOAA Next Generation Radar (NEXRAD) surface weather radar composite images from Denver, Grand Junction, and Cheyenne were collected from National Climatic Data Center for the period during the February 2003 flights. These data support precipitation patterns established by the NARR and MM5. However, although the NEXRAD images show the presence of the precipitation cells at the MSAs, the three radar images do not provide complete coverage of the CLPX area because of beam blockage by mountainous terrain.

We also obtained snow depth data from surface climatological stations at Walden, CO (North Park MSA), Steamboat Springs, CO (Rabbit Ears MSA), and Fraser, CO (Fraser MSA), for the CLPX experimental periods. During all three days in February 2002, the records show no snow on the ground during the 24-h period of the flight day at Walden, 58-cm snow depth at Steamboat Springs, and 45-cm snow depth at Fraser. In February 2003, the climatological record showed 18- to 28-cm snow depth at Walden, 72- to 85-cm snow depth at Steamboat Springs, and 33- to 38-cm snow depth at Fraser. In March 2003, the Walden climatological record showed no snow on the ground, showed 23- to 25-cm snow depth at Steamboat Springs, and showed 28- to 33-cm snow depth at Fraser during the previous 24 h.

VII. Emissivity Images

Here, we present the PSR/A and PSR/CX data sets collected during the three CLPXs. Figs. 4–6 show surface emissivity imagery for the 6.9-, 18.7-, 37-, and 89-GHz horizontal polarization channels for the North Park, Rabbit Ears, and Fraser, respectively. The image maps of the vertical polarization PSR data for all the channels and both horizontal and vertical polarization PSR data for 7.32-, 10.7-, and 21.5-GHz channels are similar to the presented images and are not shown. Hereafter, we will refer to the horizontal polarization data unless specifically stated otherwise. Also not shown are the 10-μm *IR* channel PSR data, which were used as an indication of the observed surface temperature during clear atmospheric conditions and cloud temperature in cloudy conditions. PSR emissivity maps are overlaid over the terrain elevation maps and are represented by a different color scale from the terrain elevation color scale. Thin black lines also contour terrain elevation data. The emissivity maps are organized in rows corresponding to the month and the year, i.e., for each channel, except for 6.9 GHz, there are three rows corresponding to February 2002, February 2003, and March 2003, and two to four columns corresponding to the flight observation days within the month. As noted in Section II-B, both PSR scanheads were onboard the P-3 aircraft only in March 2003; thus, Figs. 4–6 contain only one row of maps for the 6.9-GHz channel corresponding to the March 2003 measurements. Above each individual emissivity map are the observation date and the area-averaged emissivity values. We note that the 6-GHz microwave band suffers from the RFI within the USA. However, not all the frequencies within the band were affected equally. Bindlish *et al.* [22] show that during the five soil moisture experiments, where the PSR measurements were used, it was consistently noticed that the 7.32-GHz channel was the best performing channel. We randomly chose to present the 6.9-GHz channel, and, thus, we were not able to adequately recover the data at the Rabbit Ears MSA on 30 March 2003 in Fig. 5.

The maps of 6.9- and 18.7-GHz channels show detailed small-scale variations in emissivity in the range of 0.75–1.0. Larger emissivity variations for 37- and 89-GHz channels were observed with values in the range of 0.5–1.0 and 0.4–1.0, respectively. Small-scale variations within the given image map are related to the snowpack, land cover, surface temperature, and terrain elevation variations. The influence of land-cover variations is quite evident in the comparison of Fig. 1 with Figs. 4–6. For example, in Fig. 1(d) (North Park MSA), pastures and row cropland cover the central region near the riverbeds, but shrubs are prevalent away from the rivers. This central region is surrounded by mountains that are covered with deciduous forest at lower elevations, with mixed and coniferous forest at higher elevations up. In general, this distribution is reflected in Fig. 4, with lower emissivity in the central area and increasing emissivity at the edges, where land-cover changes to forest as the terrain elevation increases. These effects of pasture and row crop land showing lower emissivity and forested areas showing increased emissivity are noticeable at each MSA. In addition to the large mostly coniferous-forested areas and a small characteristically shaped pasture patch, the Fraser MSA contains alpine and barren land areas at higher elevations [Fig. 1(b)]. This distribution is reflected in Fig. 6 with high emissivity values observed over forested land and lower emissivity values in the alpine, pasture, and barren land regions of the MSA. Emissivity values are generally consistent with the land-cover types.

For a given channel and MSA, the mean emissivity differences between consecutive flights are in the 1%–3% range for 6.9-, 18.7-, and 37-GHz channels in most cases. In general, these differences were the result of fresh snowfall and surface temperature variations (Fig. 3). Two cases of anomalous behavior stand out and deserve additional explanation: 1) the February 2003 flights when the 89-GHz channel exhibited large variations on consecutive flight days due to the high sensitivity of the 89-GHz channel to the snowpack state; and 2) the 31 March 2003 flights when the 6.9-GHz channel exhibited a large drop in the brightness temperature, and the 37- and 89-GHz channels exhibit a sharp increase due to snow melt and surface soil moisture increases.

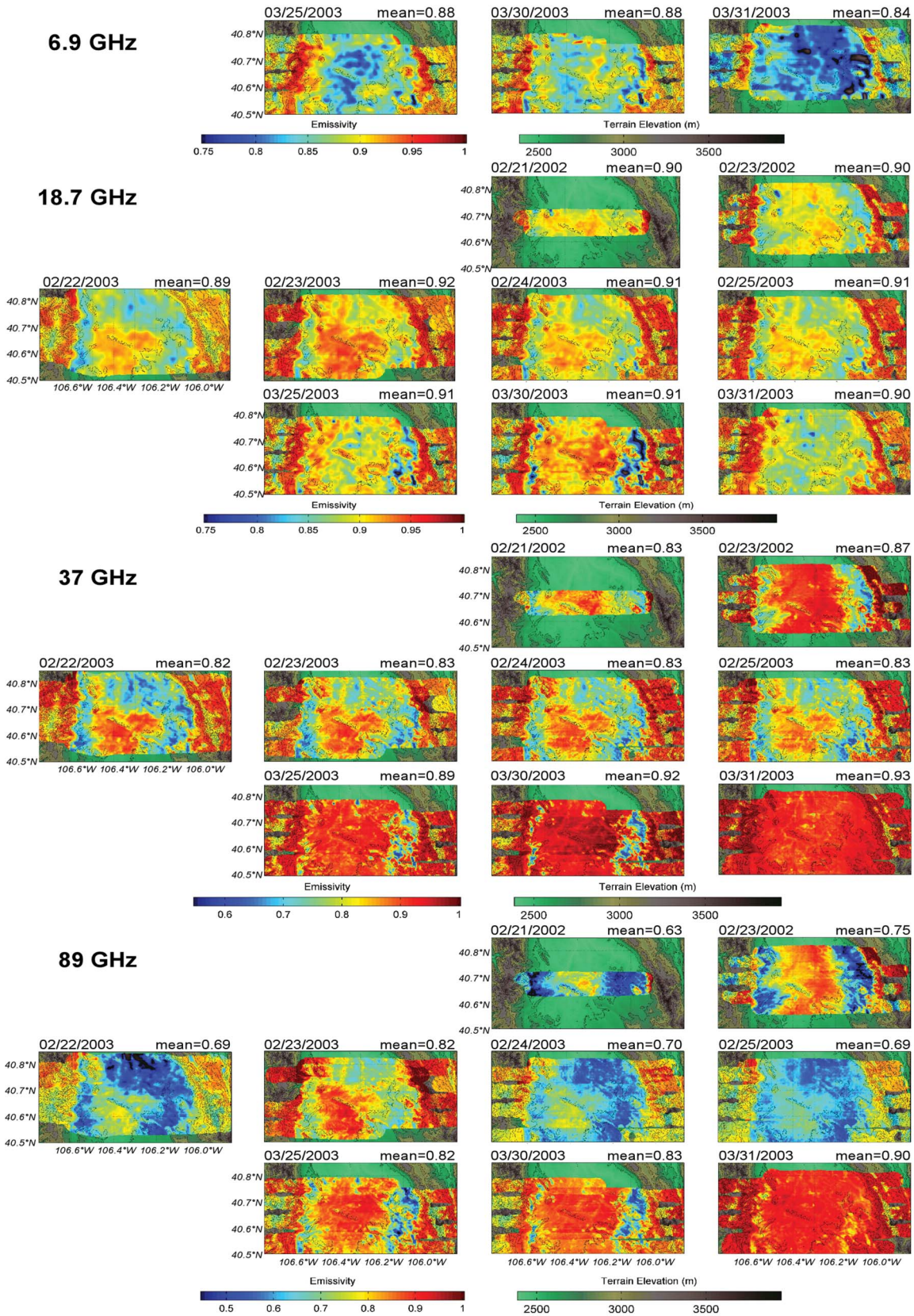

Fig. 4. PSR-observed surface emissivity images at the North Park MSA overlaid over the terrain elevation maps for the 6.9-, 18.7-, 37-, and 89-GHz H-Pol. Rows correspond to the February 2002, February 2003, and March 2003 experiments, and the columns refer to individual flight dates indicated at the upper left above each image. The mean emissivity for the entire MSA is indicated at the upper right above each image. Note that, in this presentation, there is no light source shining on the map.

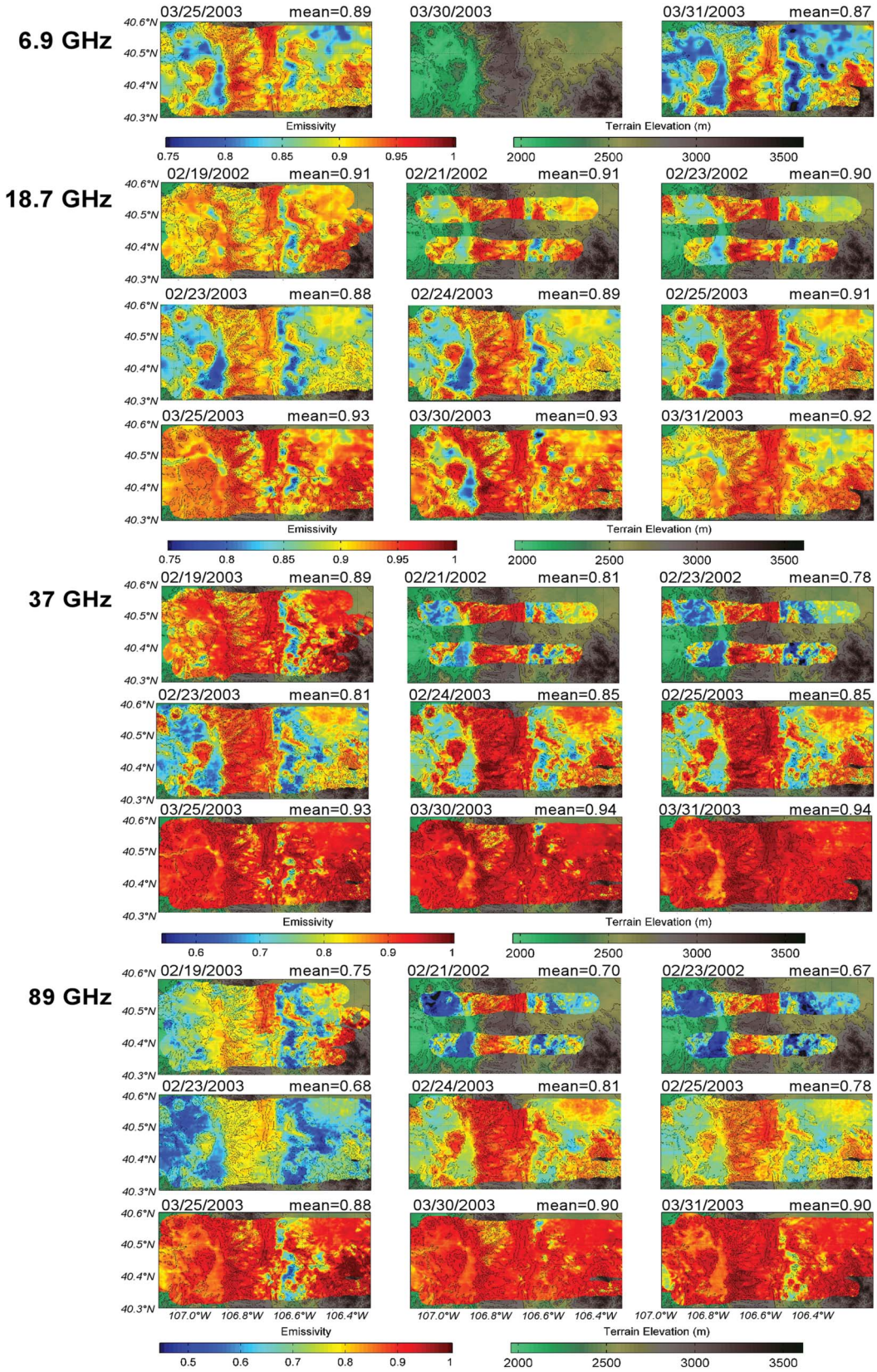

Fig. 5. Same as Fig. 4 but for the Rabbit Ears MSA.

A. *Sensitivity of the 89-GHz Channel to Precipitation*

During February 2003, the 18.7- and 37-GHz surface emissivities at North Park varied from ∼0% to 3% on consecutive flight days (Fig. 4). However, the 89-GHz channel showed a 13% increase from 22 to 23 February 2003, followed by a 12% decrease from 23 to 25 February 2003 (Fig. 4). To explain this

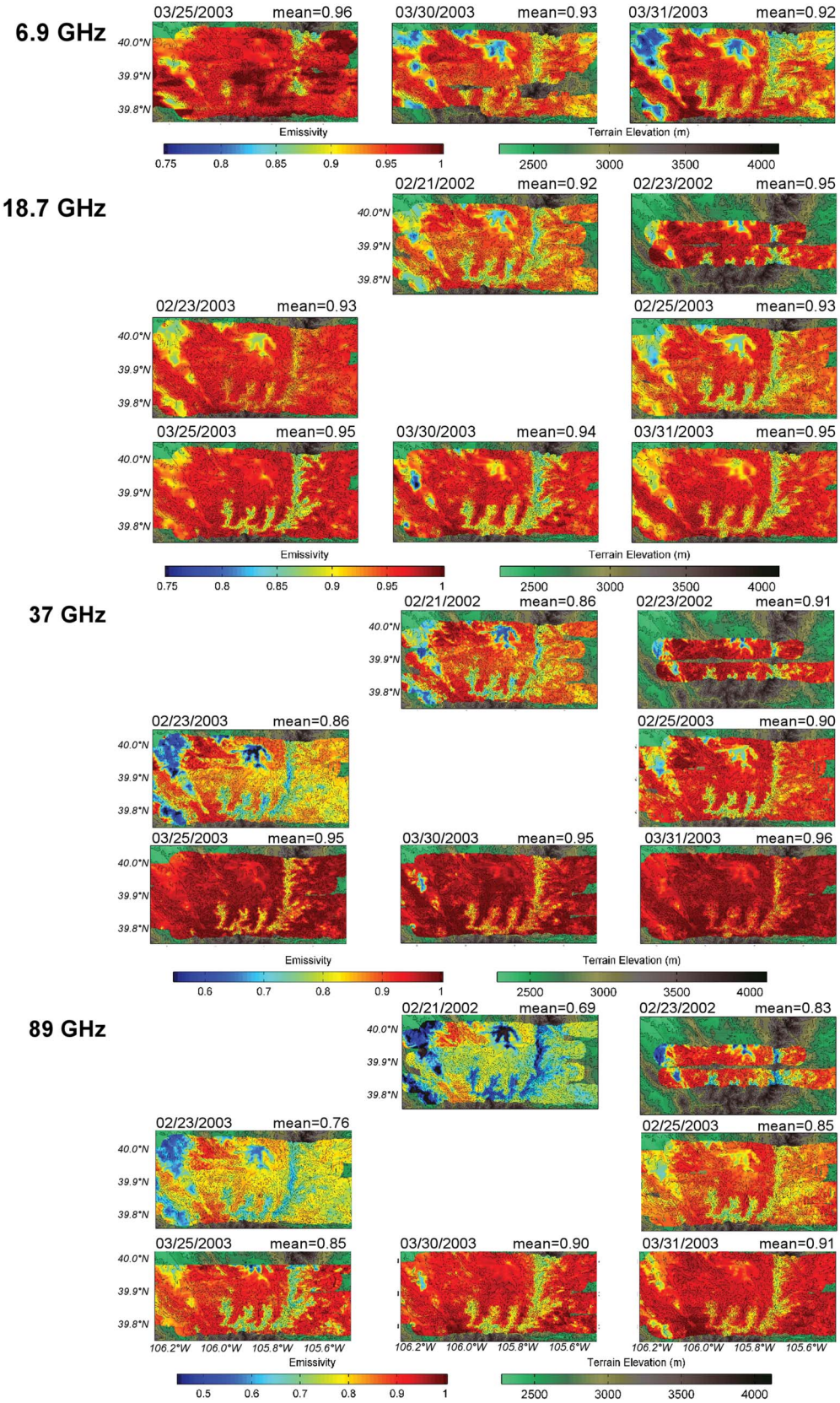

Fig. 6. Same as Fig. 4 but for the Fraser MSA.

behavior, we used the weather information from Section VI within the MRT model. On 22 February, the NARR reanalysis showed ~ 4.8 mm of accumulated three-hourly precipitation [Fig. 3(b)], and the GOES-8 data showed the presence of a deep cloud. The composite NEXRAD data from the Grand Junction, Denver, and Cheyenne radar images and the MM5

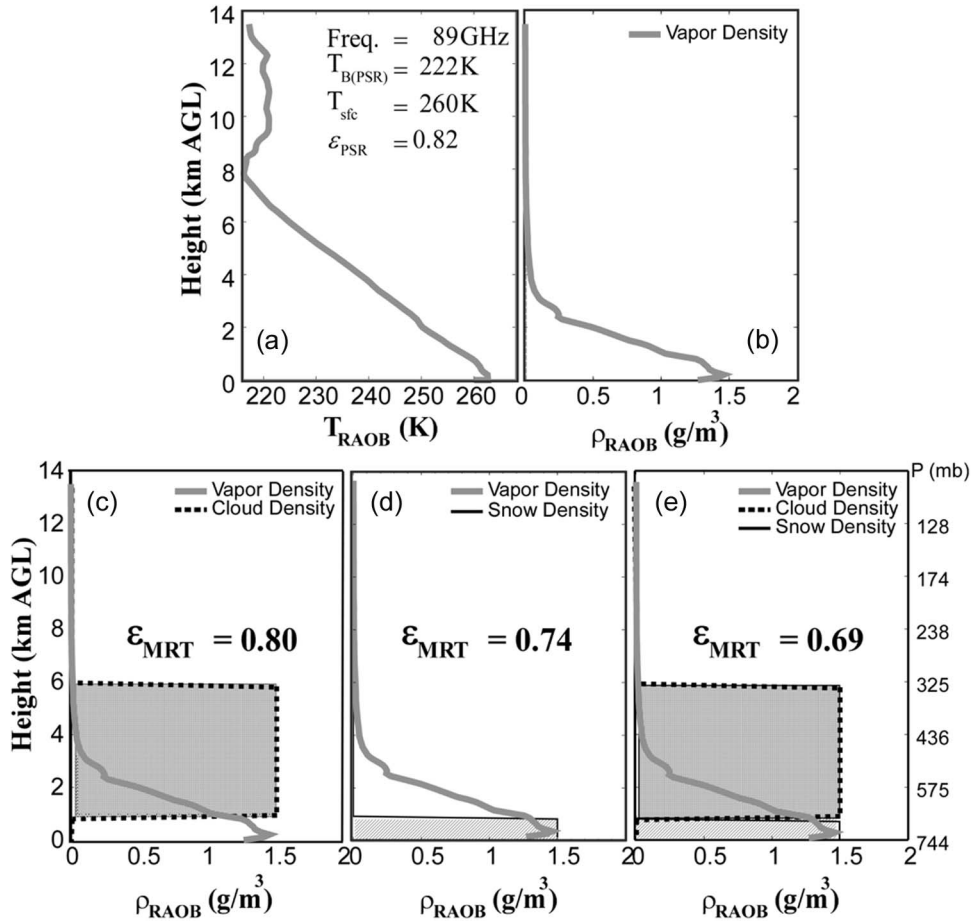

Fig. 7. MRT modeling of the 89-GHz surface emissivity on 23 February 2003 estimated to be ∼13% higher than on 22 February 2003 and 24 February 2003 at the North Park MSA. (a) Temperature profile on 23 February 2003 and the observed mean T_B, surface temperature, and mean surface emissivity. (b) Absolute humidity on 23 February 2003. (c) Absolute humidity profile in (b) with the GOES-8 observed cloud on 22 February 2003 and the value of modeled emissivity. (d) Absolute humidity profile in (b) with the shallow precipitation layer of the previous day added and the value of modeled emissivity. (e) Absolute humidity profile in (b) with both cloud and precipitation layer of the previous day added and the value of modeled emissivity.

model analysis also showed moderately strong precipitation within the North Park MSA. On 23 February 2003, the NARR analysis showed no precipitation at the North Park MSA, the GOES-8 showed that the North Park MSA was under clear weather, and the NEXRAD and MM5 showed no precipitation. Fig. 7 shows the MRT modeling on 23 February 2003 and PSR surface emissivity observations. Fig. 7(a) and (b) shows the temperature and absolute humidity profiles observed using the NWS radiosonde and the mean PSR T_B, and Fig. 7(c) shows the MRT-computed surface emissivity for the temperature and humidity profiles of 23 February if the GOES-8-observed cloud boundaries of 22 February are added. Fig. 7(d) shows the MRT-computed surface emissivity if a low shallow snow layer of the previous day is added to the MRT model, and Fig. 7(e) shows the MRT-modeled surface emissivity if both a cloud layer and a precipitation layer are added. In the absence of the knowledge of the cloud (particles other than water vapor) and snow density profile distributions, we simply assumed cloud and snow density comparable to the vapor density and constant throughout the cloud layer observed by the GOES-8 and the snow layer modeled by MM5. The MRT-modeled surface emissivity in Fig. 7(e) agrees with the observed mean surface emissivity of 22 February when the observations showed cloudiness and precipitation. During the following 2 days, observations described in Section VI indicate cloudiness and precipitation at the North Park MSA.

At the Rabbit Ears MSA, the 89-GHz mean emissivity on 24 February 2003 is 13% higher than the mean emissivity on 23 February. Although the NARR analysis shows only about 0.5 mm of three-hourly precipitation accumulation at the western edge of the MSA, the MM5 model run shows a moderate amount of precipitation, and the GOES-8 *IR* data show a shallow cloud over the entire MSA. We, again, used the MRT modeling of the 24 February temperature and humidity profiles with the addition of the NEXRAD observed cloud deck and a shallow precipitation layer on 23 February to show that the 24 February MRT-modeled emissivity agrees with the observed PSR mean surface emissivity of 23 February.

B. Spectral Response: Onset of Melting

Schanda *et al.* [23] used a data set collected in Switzerland over a 5-year period at a high-altitude (2450-m) alpine test-field site to develop a snow classification scheme by examining the spectral behavior of the microwave emissions. The scheme differentiates between dry winter snow, wet spring snow, and

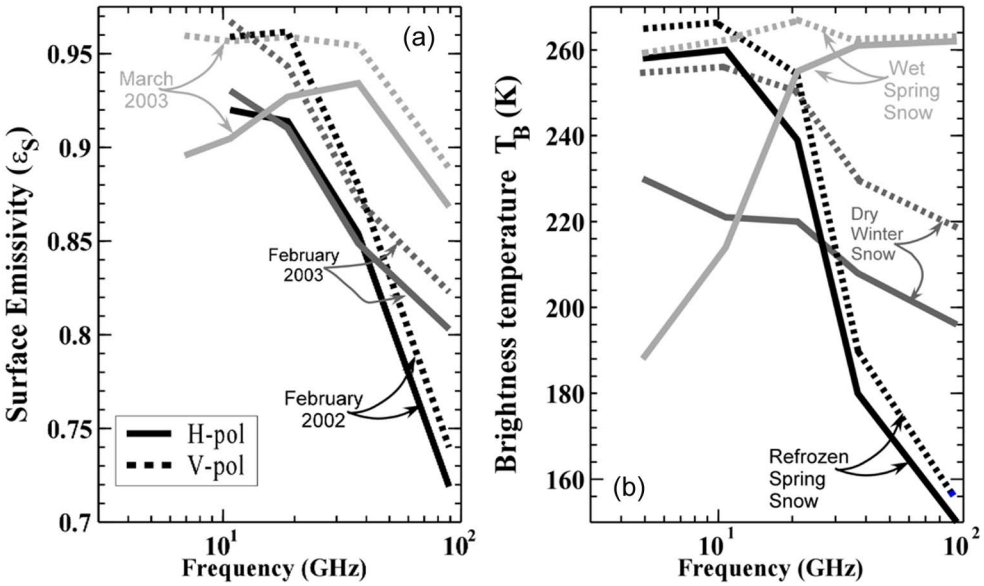

Fig. 8. Spectral behavior of the average surface emissivity observed at horizontal and vertical polarizations. (a) Emissivity averaged over all extended MSAs (Figs. 4–6) for February 2002, February 2003, and March 2003. (b) Spectral behavior of data collected (50° nadir angle) in the Alpine regions and used for SWE classification as dry winter snow, refrozen spring snow, and wet spring snow (Schanda *et al.* [23, Fig. 3]).

dry (refrozen) spring snow. Dry winter snow was described as consisting of fresh snow that has not undergone any melting metamorphism. As such, scattering is dominant as the frequency increases, and for frequencies smaller than ∼9 GHz, absorption is dominant.

Wet snow is a mixture of ice particles, water droplets, and air. Water droplets are much smaller than ice crystals, and most of the scattering occurs due to ice crystals contained inside the background medium that is a mixture of water droplets and air. Because of the high dielectric constant of liquid water compared to that of air and ice, the effective dielectric constant of the snow mixture is strongly affected by the presence of liquid water [16]. The volume absorption coefficient of the background medium increases from 0 (dry medium) to a value that is much larger than the volume scattering coefficient. Thus, even a very small amount of liquid water decreases the scattering albedo to very small values, and the snowpack approaches the nonreflecting condition of a blackbody. For frequencies higher than ∼21 GHz, the average real dielectric permittivity of wet snow is only slightly larger than that of air, and the transmissivity of air–snow boundary is only slightly smaller than 1. Consequently, the upwelling brightness temperature is only 0.92–0.99 times the surface temperature. At frequencies below ∼9 GHz, the higher permittivity of water results in higher permittivity of the snow surface; thus, the discontinuity at the surface is more significant, particularly for the horizontal polarization. As a result, brightness temperatures at lower frequencies are lower due to the water presence, and, at higher frequencies, they are closer to the surface temperature [16].

In contrast, dry refrozen snow consists of snowpack with a firm top layer that is several centimeters thick formed by freezing during clear cold nights after daytime melting [16]. Dry fresh snow and dry refrozen snow can be differentiated by looking at the emissivity difference, i.e., $\Delta\varepsilon = \varepsilon_{V\text{-pol}} - \varepsilon_{H\text{-pol}}$, at a given frequency. Dry snow crystals are nonspherical, and the polarization difference is large; however, after melting and refreezing, the nonspherical particles can acquire a preferred orientation that will affect the polarization difference. In addition, after refreezing, the snow crystals become larger causing stronger scattering at lower frequencies.

Fig. 8(a) shows a PSR spectral plot of horizontal and vertical polarization surface emissivity values observed at a 55° nadir angle and averaged over all extended MSAs [Fig. 1(a)] for February 2002, February 2003, and March 2003. Fig. 8(b) shows spectra for the three typical snow-cover conditions described above [23]. The spectral behavior of the PSR data [Fig. 8(a)] is similar to that of the classification model [23] [Fig. 8(b)]. The February 2002 curve shows a pattern that is consistent with dry refrozen snow, whereas the February 2003 curve shows a pattern that is consistent with the dry fresh snow. The surface emissivity difference between vertical and horizontal polarization of $\Delta\varepsilon_S$ for February 2003 is 17%, which is close to 18%–25% of ΔT_B for the dry snow in Fig. 8(b). March 2003 shows a pattern that is consistent with the wet snow curve in Fig. 8(b), as expected at the onset of melting. Although we did not separate snow-covered and snow-free regions when computing the data in Fig. 8(a), the PSR data clearly show consistency with the snow classification model. Specifically, the images in Figs. 4–6 for the 6.9-GHz channel for March 2003 show large areas of low emissivity, indicating the presence of water, and the images in Figs. 4–6 for the 37- and 89-GHz channels show large emissivity values that are close to that of the land emissivity, again indicating the presence of water. Indeed, on 31 March, an observer onboard the aircraft noted, "Sun glint due to melting snow observed at all three MSAs."

Spectral plots of average emissivity for individual flight days show patterns that are much closer to those in Fig. 8(b) with overall emissivity variations in the range of 0.6–0.995. Note that the strongest melting occurred at North Park on 31 March 2003. During this day, the lowest emissivities at 6.9 GHz were observed (Fig. 4), as expected.

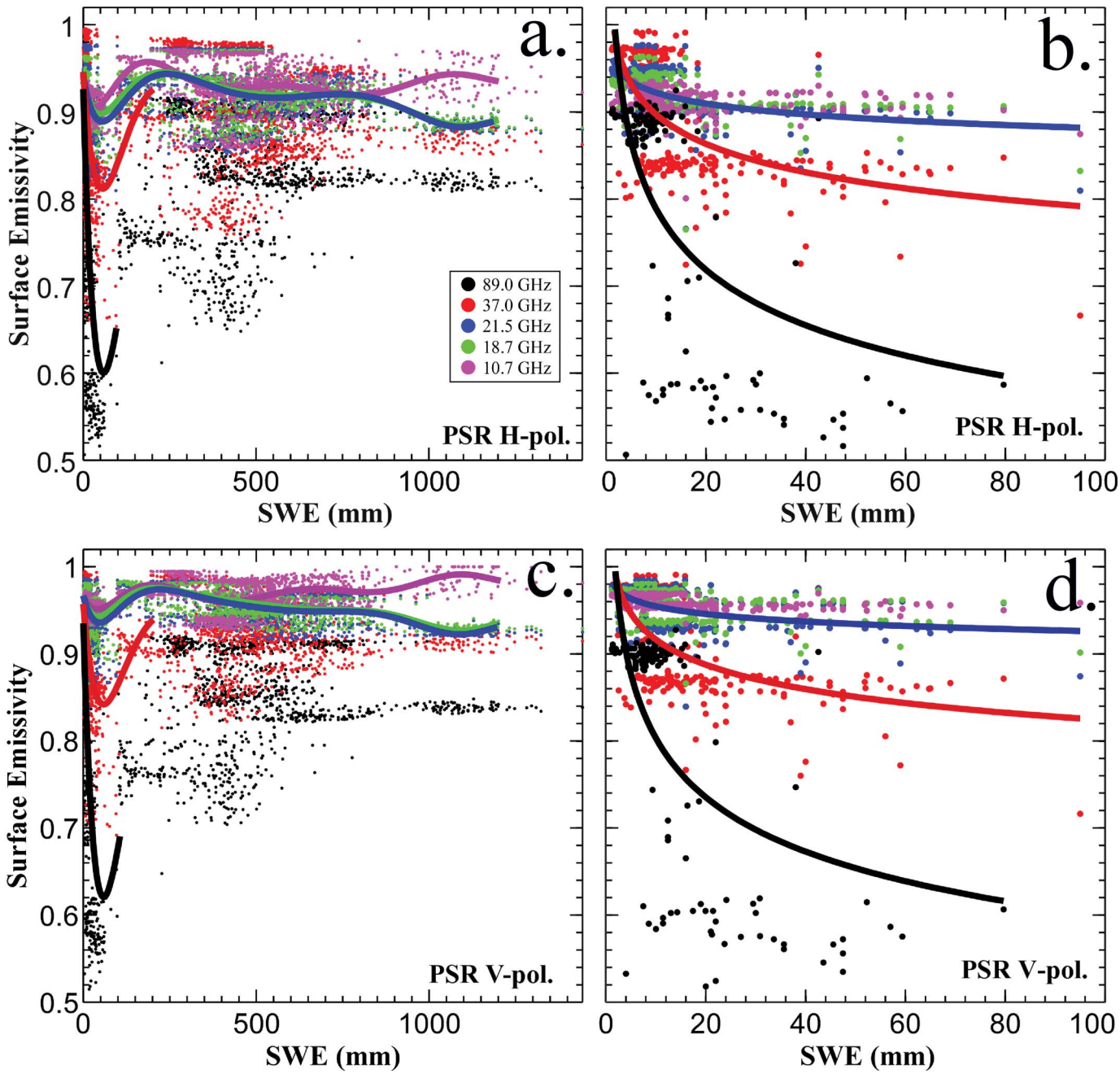

Fig. 9. Surface emissivity versus ground-based measurement of the SWE for PSR 10.7-, 18.7-, 21.5-, 37-, and 89-GHz channels. (a) For the horizontal polarization PSR data of the entire CLPX comparison data set of 2304 collocated points, which includes all wet data. (b) For the horizontal polarization PSR data of the filtered CLPX comparison data set of 224 collocated points. (c) Same as in (a), but for the vertical polarization PSR data. (d) Same as in (b), but for the vertical polarization PSR data. Solid lines in (a) and (c) represent a tenth degree polynomial fit to each of the frequency data, with fitted curves for 89- and 37-GHz channels removed beyond the penetration depth of each channel. Solid lines in (b) and (d) represent a fit of a form $y = Cx^n$ for 10.7-, 18.7-, and 21.5-GHz channels altogether and for 37- and 89-GHz channels.

VIII. SWE

A retrieval algorithm is needed to translate the microwave measurements shown in Figs. 4–6 into maps of the SWE. Application of the well-known Chang algorithm [3] to the CLPX PSR measurements did not produce SWE estimates that agreed with the *in situ* measurements. Stankov *et al.* [10] used CLPX PSR data and the HUT semiempirical model to show that the CLPX microwave brightness temperature data generally exhibit the expected frequency dependence. They then used the CLPX and HUT brightness temperature data set to derive the SWE retrieval algorithm. Here, we apply their methods to the CLPX emissivity measurements to develop a SWE retrieval algorithm and use the derived algorithm to obtain maps of SWE fields for all the extended MSAs.

A. SWE Algorithm Development

Fig. 9(a) and (c) shows plots of the PSR horizontal and vertical polarization emissivity versus the ground-based

TABLE III
CORRELATION ANALYSIS FOR THE 224 POINTS FILTERED DATA. A_1 IS THE COEFFICIENT IN THE BEST-FIT REGRESSION LINE THAT REPRESENTS THE MICROWAVE RESPONSE TO SWE, R IS THE CORRELATION COEFFICIENT, AND RMS IS THE ROOT-MEAN-SQUARE VALUE OF THE REGRESSION FIT

	PSR			Hallikainen [25]: South			Hallikainen [25]: North		
	A1	**R**	**rms**	**A1**	**R**	**rms**	**A1**	**R**	**rms**
10.7H	-0.016	-0.100	2.88	0.012	0.040	6.30	-0.048	-0.210	3.40
10.7V	-0.026	-0.361	1.05	0.038	0.160	3.80	-0.005	-0.120	2.10
18.7H	-0.072	-0.330	3.29	-0.048	-0.130	8.10	-0.113	-0.430	4.90
18.7V	-0.059	-0.438	1.95	-0.002	-0.010	4.90	-0.041	-0.190	3.00
21.5H	-0.088	-0.370	3.52	-0.027	-0.020	16.20	-0.177	-0.100	14.90
21.5V	-0.083	-0.476	2.47	0.040	0.030	12.70	-0.052	-0.060	14.70
37.0H	-0.258	-0.508	6.99	-0.159	-0.300	10.10	-0.300	-0.540	8.20
37.0V	-0.248	-0.538	6.22	-0.123	-0.330	6.80	-0.226	-0.550	5.90
89.0H	-0.934	-0.659	14.52						
89.0V	-0.945	-0.661	14.54						
10.7H - 37H	0.242	0.509	6.55						
10.7V - 37V	0.218	0.550	5.33	0.162	0.490	5.20	0.233	0.630	5.10
10.7V - 37H	0.233	0.511	6.26	0.199	0.420	8.40	0.310	0.590	7.40
18.7H - 37H	0.186	0.535	4.70	0.113	0.450	4.00	0.193	0.570	4.90
18.7V - 37V	0.189	0.555	4.52	0.124	0.560	3.40	0.187	0.620	4.30
18.7V - 37H	0.199	0.515	5.29	0.162	0.450	6.30	0.260	0.590	6.40
21.5H - 37H	0.165	0.538	4.27						
21.5V - 37V	0.169	0.546	4.03	0.110	0.470	3.90	0.159	0.560	4.10
21.5V - 37H	0.175	0.501	4.82	0.148	0.400	6.60	0.237	0.570	6.10
Func 1	0.189	0.551	4.54	0.119	0.530	3.40	0.191	0.610	4.50
10.7H - 89H	0.948	0.662	14.47						
10.7V - 89V	0.891	0.659	13.71						
18.7H - 89H	0.839	0.664	12.75						
18.7V - 89V	0.853	0.658	13.14						
21.5H - 89H	0.817	0.663	12.43						
21.5V - 89V	0.821	0.655	12.78						
37H - 89H	0.566	0.662	8.63						
37V - 89V	**0.599**	**0.661**	**9.16**						
Func1=0.5(18H-37H+18V-37V)									

measurements of SWE for 10.7, 18.7, 21.5, 37, and 89 GHz for the entire 2304 (Section V) point data set. The measured SWE values extended from 0 to 1445 mm, and the observed emissivity shows a large degree of scatter at all frequencies. A 10° polynomial (solid lines) was fitted to the data at each frequency. An initial sharp drop in emissivity up to SWE $=\sim 80$ mm, particularly for the 37- and 89-GHz channels, takes a sharp turn upward with an increasing SWE. However, because the penetration depth of the 89- and 37-GHz channels is quite small, about SWE $= 80$ mm and SWE $= 200$ mm, respectively, we show the fit only up to the penetration depth SWE values for those channels in Fig. 9(a) and (c). The lower frequencies show a similar but attenuated response. Matzler *et al.* [24] and Schanda *et al.* [23] show data exhibiting similar patterns. They attributed the upturn in the T_B (or emissivity) versus SWE to the prevalence of larger snow grains in the shallow snowpack that affects the snowpack albedo. Indeed, averaging all the grain size data, where SWE ≤ 80 mm, we obtain a grain size mean radius of $r = 0.2439$ mm, whereas averaging all the grain size data for SWE > 100 mm, we obtain a mean radius of $r = 0.1883$ mm. Thus, we confirmed that the above explanation for the upturn also holds for the PSR data.

By applying several filters to the complete colocated data set, we extracted a subset consisting of dry snow with uniform characteristics. The filters applied were 1) to exclude all points with macrovegetation according to land usage data; 2) to exclude all points with wet or moist snow according to *in situ* data; and 3) to remove all points with surface or maximum snow-pit temperature above or equal to zero [10]. Fig. 9(b) and (d) shows the same plot as in Fig. 9(a) and (c), respectively, but for the filtered data set of 224 points. All data points remaining after filtering were located at the North Park MSA, and they exhibited a significantly reduced degree of scatter compared to Fig. 9(a) and (c). Since emissivity values for the 10.7-, 18.7-, and 21.5-GHz channels overlapped, we fitted one curve of the form $y = Cx^n$ to those points. We also separately fitted a power curve to the 37-GHz data and to the 89-GHz data. The fitted curves for the 37- and 89-GHz channels show a sharp drop in emissivity with an increasing SWE up to ~80 mm. Curves fitted to the lower frequency channel data do not show nearly such a significant drop in emissivity with an increasing SWE, thus illustrating the basic multispectral relationship that is useful for SWE retrieval under such low SWE burdens. We note that the fitted curves in Fig. 9(b) show a behavior that is very similar to that of the theoretical curves in [3] over this low range of SWE values.

Using the filtered data set, we analyzed the relationships between the SWE and all emissivity/T_B two-frequency difference combinations $(f_{\text{lower}} - f_{\text{higher}})$. We estimated the best-fit regression line in the form of $y = A_0 + A_1 \times$ SWE, where A_0 varies with emissivity/T_B function and the snow conditions, and A_1 gives the microwave response to the SWE. We computed the correlation coefficient R and the rms values of the regression and compared them with the results from a similar analysis performed using Nimbus 7 SMMR data from Finland [25]. Table III shows that the values of A_1 and R coefficient for the CLPX PSR data are similar to the Finland [25] data for most

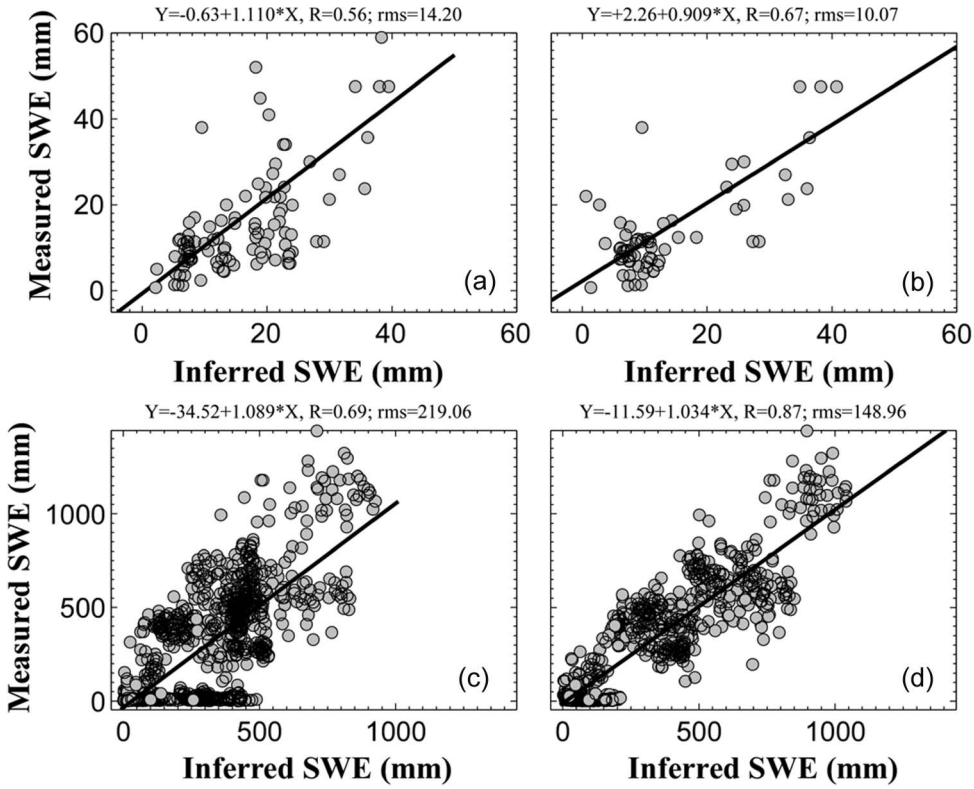

Fig. 10. Comparison of the observed SWE to the SWE modeled by multiple linear regression for PSR data (a) using (8), (b) using (9), (c) using (10), and (d) using (11).

of the difference functions, and that all frequency difference functions showed an equally strong microwave response to the SWE with the rms values indicating a relatively large scatter. The correlation coefficient values are all in the significant range. Based on these results, we used least square multiple linear regression to fit the SWE as a function of the emissivity differences $\Delta\varepsilon$. The first case consisted of the differences between lower frequency channels, i.e., the 10.7-, 18.7-, and 21.5-GHz channels and the 37-GHz channel, and the second case consisted of the differences between lower frequency channels, i.e., the 10.7-, 18.7-, 21.5-, and 37.0-GHz channels and the 89-GHz channel. Both the filtered (224 points) and complete (2304 points) data sets were considered. Using multiple regression on the filtered data set gives a set of coefficients that is valid for the SWE values between 0 and 80 mm, and applying multiple regression to the entire data set gives a set of coefficients for the SWE values up to 1445 mm.

For the filtered data set, the multiple regression fit in the first case is given by

$$\begin{aligned}\mathrm{SWE_{calc}} = &+16 - 1464(\varepsilon_{10V} - \varepsilon_{37V}) \\ &+ 4908(\varepsilon_{18V} - \varepsilon_{37V}) - 3681(\varepsilon_{21V} - \varepsilon_{37V}) \\ &+ 410(\varepsilon_{10H} - \varepsilon_{37H}) - 1129(\varepsilon_{18H} - \varepsilon_{37H}) \\ &+ 1020(\varepsilon_{21H} - \varepsilon_{37H}) \end{aligned} \tag{8}$$

and in the second case, it is given by

$$\begin{aligned}\mathrm{SWE_{calc}} = &+13 - 2830(\varepsilon_{10V} - \varepsilon_{37V}) \\ &+ 9310(\varepsilon_{18V} - \varepsilon_{37V}) - 472(\varepsilon_{21H} - \varepsilon_{37H}) \\ &- 6445(\varepsilon_{21V} - \varepsilon_{89V}) + 723(\varepsilon_{10H} - \varepsilon_{89H}) \\ &- 2177(\varepsilon_{18H} - \varepsilon_{89H}) + 1948(\varepsilon_{21H} - \varepsilon_{89H}) \\ &+ 5905(\varepsilon_{37V} - \varepsilon_{89V}). \end{aligned} \tag{9}$$

For the full data set, the multiple regression fit in the first case is given by

$$\begin{aligned}\mathrm{SWE_{calc}} = &+471 + 1937(\varepsilon_{10V} - \varepsilon_{37V}) \\ &- 33\,881(\varepsilon_{18V} - \varepsilon_{37V}) + 20\,488(\varepsilon_{21V} - \varepsilon_{37V}) \\ &+ 4698(\varepsilon_{10H} - \varepsilon_{37H}) + 9612(\varepsilon_{18H} - \varepsilon_{37H}) \\ &- 4468(\varepsilon_{21H} - \varepsilon_{37H}) \end{aligned} \tag{10}$$

and in the second case, it is given by

$$\begin{aligned}\mathrm{SWE_{calc}} = &+410 + 23\,192(\varepsilon_{10H} - \varepsilon_{37H}) \\ &- 8190(\varepsilon_{21H} - \varepsilon_{37H}) + 4595(\varepsilon_{10V} - \varepsilon_{89V}) \\ &- 15\,194(\varepsilon_{18V} - \varepsilon_{89V}) + 7050(\varepsilon_{21V} - \varepsilon_{89V}) \\ &- 22\,679(\varepsilon_{10H} - \varepsilon_{89H}) + 10\,525(\varepsilon_{18H} - \varepsilon_{89H}) \\ &+ 14\,513(\varepsilon_{37V} - \varepsilon_{89V}). \end{aligned} \tag{11}$$

We randomly selected half of each data set for the regression and used the remaining half to obtain the SWE from the microwave observations; we then compared the inferred SWE with the measured SWE. Fig. 10 shows the agreement between the measured SWE and the SWE inferred from (8)–(11). The linear regression fit between the measured and calculated SWEs in the form $Y = A_0 + A_1X$ is shown as a black line and in the equation form above each panel of Fig. 10. The coefficient A_1 is approximately 1 in all cases, the correlation coefficient R varies from 0.56 to 0.87, and the rms error varies from 10% to 16% of the maximum SWE.

Fig. 11 shows examples of inferred SWE images for the 22 February 2003 North Park, 30 March 2003 Rabbit Ears, and 30 February 2003 Fraser MSAs using (8) and (10). Since the 30-m-resolution USGS land-cover data were available, it

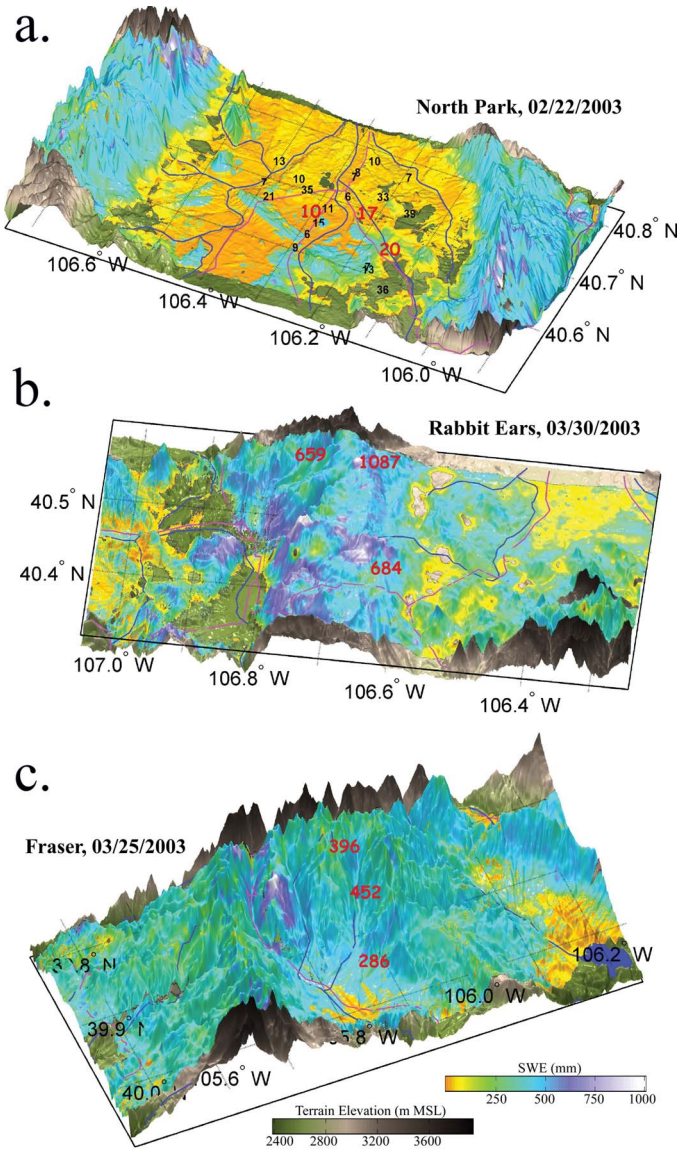

Fig. 11. Examples of SWE images computed using (8) and (10) for 22 February 2003 North Park MSA, 30 March 2003 Rabbit Ears MSA, and 25 March 2003 Fraser MSA. Red numbers represent average SWE values for each ISA, and black numbers at North Park MSA represent every third measurement from the extended snow pits. An external light was added as a source to each of the maps, thus creating shadows and enhancing relief features.

was possible to test for the land cover at each pixel and apply either the formulas corresponding to the filtered data set for cases where no macrovegetation was present or the general set of formulas for all other land-usage types. This procedure was based on the fact that the SWE < 80-mm retrieval algorithms were developed using the filtered data set, associated with data from areas in North Park of low vegetation. Fig. 11(a) shows a PSR inferred SWE map at North Park with an average SWE observed at each ISA for that day (red numbers) and the individual SWE measurements at the extended snow pits (black numbers). Fig. 11(b) and (c) is the same as Fig. 11(a), but for Rabbit Ears MSA and Fraser MSA, respectively. As expected, there is a good agreement between the PSR-inferred SWE and ground-based SWE observations.

In general, vertical polarization channel pairs contributed most in (8) and (10) with 18V- to 37V-GHz difference con-

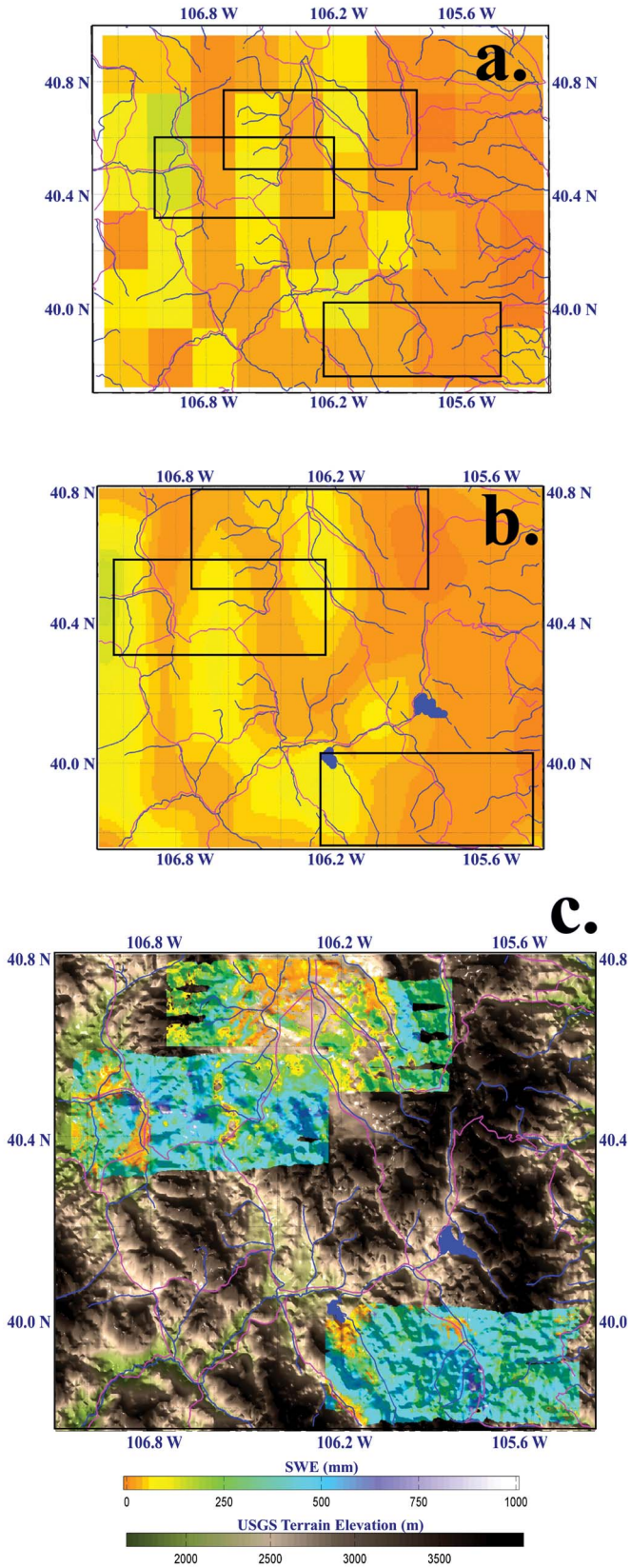

Fig. 12. (a) AMSR-E SWE computed using the Chang formula [3]. (Black line squares) MSA positions within the large AMSR-E covered area. (b) Same as in (a), but AMSR-E data interpolated onto a 1-km grid. (c) PSR SWE computed using (8) and (10) for the North Park, Rabbit Ears, and Fraser MSAs draped over the terrain of the large area covered by AMSR-E data in (a).

TABLE IV
COMPARISON OF THE SWE COMPUTED FROM (8)–(11), CHANG FORMULA [3], AND GAMMA OBSERVATIONS [4]

MSA	Date	PSR SWE1 Eqs, 8 &10		PSR SWE2 Eqs. 9 & 11		PSR Chang		Gamma		SWE1-SWE2		SWE1-Chang		SWE1-Gamma		Gamma-Chang	
		Mean	Std	Mean	Std	Mean	Std	Mean	Std	Mean	STD	Mean	STD	Mean	Std	Mean	Std
North Park	Feb. 2002	73.0	96.2	106.0	91.1	84.8	55.0			-45.6	89.9	-17.2	113.1				
	Feb. 2003	158.6	134.7	267.0	172.1	92.3	53.7	45.7	6.5	-111.0	173.5	43.0	172.4	35.6	131.1	-47.1	54.1
	Mar. 2003	127.9	114.9	302.7	150.3	33.0	31.7			-144.3	163.0	106.4	122.0				
	Total-NP	**119.8**	**83.9**	**225.2**	**137.8**	**70.0**	**46.8**	**45.7**	**6.5**	**-96.2**	**142.1**	**44.1**	**135.8**	**35.6**	**131.1**	**-47.1**	**54.1**
Rabbit Ears	Feb. 2002	171.3	117.8	234.5	132.0	102.8	68.5			-136.6	134.4	28.8	167.9				
	Feb. 2003	260.5	161.4	369.9	191.5	56.5	41.1			-112.0	192.3	193.4	193.3				
	Mar. 2003	277.0	160.5	453.2	163.7	38.7	31.6	315.8	66.2	-176.0	178.7	242.7	179.0	143.2	185.1	306.9	70.2
	Total-RE	**236.3**	**146.6**	**353.5**	**162.4**	**66.0**	**47.1**	**315.8**	**66.2**	**-117.3**	**168.5**	**155.0**	**180.1**	**143.2**	**185.1**	**306.9**	**70.2**
Fraser	Feb. 2002	134.8	94.1	126.0	82.9	61.5	51.5			-8.5	84.7	40.5	128.8				
	Feb. 2003	251.9	111.1	287.9	100.0	55.0	38.2			-51.2	131.8	183.8	149.4				
	Mar. 2003	327.2	129.7	327.8	128.8	20.7	18.8	290.0	46.5	15.9	117.2	322.0	132.2	110.3	116.6	282.7	50.2
	Total-F	**238.0**	**111.6**	**247.2**	**103.9**	**45.8**	**36.2**	**290.0**	**46.5**	**-14.6**	**111.2**	**182.1**	**136.8**	**110.3**	**116.6**	**282.7**	**50.2**
	Total-CLPX	***198.0***	***114.0***	***275.0***	***134.7***	***60.6***	***43.3***	***217.2***	***39.7***	***-76.0***	***140.6***	***127.0***	***150.9***	***96.4***	***144.3***	***181.0***	***58.2***

TABLE V
COMPARISON OF THE TOTAL WATER STORAGE IN EACH MSA COMPUTED FROM PSR AND AMSR-E

	AMSR-E Volume (km^3)	PSR Volume (km^3)	PSR – AMSR (km^3)	PSR/AMSR
North Park	0.2046	0.4504	0.2458	2.20
Rabbit Ears	0.2073	0.9592	0.7519	4.63
Fraser	0.1084	0.8526	0.7443	7.87

tributing the most, followed by 21V–37V and 10V–37V GHz. Horizontal polarization difference pairs were markedly less significant in (8) and (10). Similarly, in (9) and (11), channel pairs of 18V–37V, 18V–89V, and 37V–89V GHz showed the largest contribution; however, the contribution from the horizontal polarization channel pairs was also significant.

We computed the SWE maps for all the experimental days in Figs. 4–6 using (8) and (10) in the same manner as in the Fig. 11 examples. PSR SWE image maps show a pattern that follows the weather conditions discussed in Section VI. The February 2002 map shows a dry season at all MSAs, but the amount of the SWE varies within a given MSA. February 2003 was a normal year consistent with precipitation patterns described in Section VI, and March 2003 shows melting at the lower altitudes and pockets of a high SWE at higher elevations.

B. SWE Comparisons

In addition to computing SWE image maps using (8) and (10), we computed SWE image maps from PSR data using (9) and (11) and using the well-known Chang formula [3]. Chang's formula is based on the differences between the 18- and 37-GHz horizontal polarization data. We also computed SWE image maps from the gamma spectroscopy data using a kriging interpolation scheme to interpolate the integrated gamma flight line data to the PSR data locations. We then computed the area mean of the computed SWE and the mean of the pixel-by-pixel differences between various combinations of the SWE computed with each formula and differences with the gamma-observed SWE. Table IV shows a summary of those computations for each season and each MSA, as well as the mean of all seasons for each MSA and an average of all MSAs for all seasons.

For each MSA, the pattern of 2002 being a dry year with the increased SWE amounts for the 2003 emerges. The all-season mean for the North Park MSA is the smallest compared to the Rabbit Ears and Fraser MSAs for the SWE computed from (8) and (10), and from (9) and (11). The overall mean SWE computed using Chang's formula is significantly smaller than the SWE computed using regression equations (8)–(11) and from the gamma-observed SWE. This pattern is also reflected in the difference columns. The SWE based on (8) and (10) minus the SWE based on Chang's formula shows the smallest difference for the North Park MSA, and that difference increases with the Rabbit Ears and Fraser MSAs. The same pattern is shown in the SWE from (8) and (10) compared with the gamma SWE and the gamma SWE minus the Chang formula SWE. Overall, the SWE based on (8) and (10) is always smaller than the SWE computed based on (9) and (11), and the differences between the gamma SWE and the Chang SWE are the largest.

Fig. 12(a)–(c) shows a comparison of the AMSR-E and PSR-inferred SWE for the large area containing all three MSAs. AMSR-E [Fig. 12(a)] shows an SWE computed using the Chang formula with only eight measurement points for each MSA, whereas the PSR measurements [Fig. 12(c)] show a 100-m spatial resolution with small-scale variations being significant. Fig. 12(b) shows an SWE computed using the AMSR-E Chang formula, but interpolated onto the 100-m-resolution grid. Fig. 12(a) and (b) shows an SWE computed using the Chang formula with the AMSR-E observations that are used in many daily climatological studies. Fig. 12(c) shows an SWE computed using (8) and (10) for each individual MSA. Comparing Fig. 12(a) and (c) shows that the SWE computed using the Chang formula does not show high SWE areas at the Rabbit Ears and Fraser MSAs, as well as areas of no snow cover in the North Park MSA.

To estimate the effect of underestimating the SWE using the Chang formula, we interpolated AMSR-E estimates of the SWE to the PSR grid of SWE observations and computed the total volume of water storage (integrated SWE) for each MSA from the AMSR-E and from the PSR for the examples given in Fig. 12(a) and (c) (Table V). If the empirical PSR estimates are taken as the truth, on this particular day, the total water content from satellite measurements underestimated the total volume of water storage by a factor of two for North Park, a factor of five for Rabbit Ears, and a factor of eight for Fraser. To place these differences into perspective, the combined difference between the PSR and AMSR-E estimates at the Rabbit Ears and Fraser MSAs (1.5 km^3) is approximately 5% of the total capacity of the Colorado River's Lake Powell, the second largest manmade reservoir in the USA and a critical water storage facility for southwestern USA.

IX. Conclusion

The PSR and related ancillary observations made during the 2002 and 2003 CLPX campaigns provided a comprehensive high-resolution passive microwave data set that has been used for the development of snowpack parameter radiative transfer studies and for retrieval algorithm development. The emissivity modes observed by the PSR closely match those catalogued in [23] for three major snow classes (dry, wet, and refrozen) across a frequency range from $\sim$6 to 89 GHz. The empirical relationships between emissivities and SWEs found in this study also closely match those found in [3] for moderately low SWE values (< 80 mm).

The new retrieval algorithms based on spectral emissivity differences developed from the PSR data are similar in principle to the Chang algorithm [3], but include frequencies other than horizontal polarization 18.7 and 37 GHz. These algorithms are believed to be more accurate than Chang's original algorithm for airborne mapping purposes, although the application of these algorithms to satellite mapping would require the consideration of the large footprint sizes that would be available at the lower frequency channels. The use of the 89-GHz channel provides improved accuracy under dry snow conditions and a small SWE, and would also provide an improved surface resolution from the space. However, this channel suffers from enhanced variability under wet and refrozen snow conditions. In all cases, at larger SWE values, we find that the variability of the SWE–emissivity relationship substantially increases and renders the accurate retrieval of the SWE using single-look multispectral data difficult.

The CLPX experiment also provided a unique opportunity to develop airborne SWE mapping techniques using conical scanning radiometry. The techniques developed included the geolocation over mountainous terrain, the surface emissivity referencing and facet angle correction, the incorporation of ancillary data, and the use of a broad set of channels to provide optimal SWE estimation accuracy. The technique provides an alternate means of SWE mapping with a significantly better spatial resolution than gamma radiation techniques, albeit directly useful only at low SWE values. The extension of passive techniques—whether airborne or spaceborne—to moderate-to-high values of the SWE is expected to require regular assimilation of passive microwave radiance into snowpack models to provide a means of accumulating the SWE within the snow burden underlying freshly observed snow layers, as well as handling snow emissivity changes due to melt and refreeze. Such models will also facilitate the better use of a W-band channel for an improved sensitivity and spatial resolution and a C-band channel for soil moisture estimation during spring melt.

The results of our analysis suggest the importance of exploiting more frequency information than has been traditionally used for the estimation of the SWE. Moreover, although it is not surprising that an algorithm empirically tuned to local conditions would perform better than a general algorithm developed for global application, it is clear that the differences in performance can be large enough to have hydrologic significance. This paper suggests that new algorithmic methods need to be developed and implemented that better account for local conditions, perhaps using land-cover information as one means of improving performance.

Acknowledgment

The authors would like to thank K. Elder and the CLPX field team for their efforts in collecting the *in situ* data, M. Klein for his exceptional engineering of the PSR system and airborne data collection, M. Parsons and M. J. Brodzik for their outstanding data management support during and following CLPX, C. A. Hiemstra for providing the 30-m-resolution USGS Land Cover data, D. Birkenheuer for providing LAPS data in near real time, and S. Oncley for providing the ISFF observations. They would also like to thank W. Madsen and C. Smith for their assistance with accessing many different data sets.

References

[1] D. W. Cline, K. Elder, B. Davis, J. Hardy, G. E. Liston, D. Imel, S. H. Yueh, A. J. Gasiewski, G. Koh, R. L. Armstrong, and M. Parsons, "Overview of the NASA cold land processes field experiment (CLPX-2002)," in *Proc. SPIE—Microwave Remote Sensing Atmosphere Environment III*, C. D. Kummerow, J. Jiang, and S. Uratuka, Eds., 2002, vol. 4894, pp. 361–372.

[2] R. A. Anthes, B. Moore, III, J. G. Anderson, S. K. Avery, E. J. Barron, O. B. Brown, Jr, S. L. Cutter, R. DeFries, W. B. Gail, B. H. Hager, A. Hollingsworth, A. C. Janetos, K. A. Kelly, N. F. Lane, D. P. Lettenmaier, B. Marcus, A. M. Mika, W. M. Washington, M. L. Wilson, and M. L. Zoback, *Earth Science and Applications from Space: National Imperatives for the Next Decade and Beyond*. Washington, DC: Nat. Academy Press, Feb. 2007.

[3] A. T. C. Chang, "Nimbus-7 SMMR snow cover data," *Glaciol. Data*, vol. GD-18, pp. 181–187, 1986.

[4] D. W. Cline, R. Armstrong, R. Davis, K. Elder, and G. Liston, "NASA Cold Land Processes Field Experiment Plan 2002–2004," *Cold Land Processes Working Group: NASA Earth Science Enterprise. Land Surface Hydrology Program*, p. 152, May 2001.

[5] J. E. Vogelmann, S. M. Howard, L. M. Yang, C. R. Larson, B. K. Wylie, and N. Van Driel, "Completion of the 1990s National Land Cover data set for the conterminous United States from Landsat Thematic Mapper data and ancillary data sources," *Photogramm. Eng. Remote Sens.*, vol. 67, no. 6, pp. 650–662, 2001.

[6] J. G. Piepmeier and A. J. Gasiewski, "High-resolution passive polarimetric microwave mapping of ocean surface wind vector fields," *IEEE Trans. Geosci. Remote Sens.*, vol. 39, no. 3, pp. 606–622, Mar. 2001.

[7] T. J. Jackson, R. Bindlish, A. J. Gasiewski, B. B. Stankov, M. Klein, E. G. Njoku, D. Bosch, T. L. Coleman, C. A. Laymon, and P. Starks, "Polarimetric scanning radiometer C- and X-band microwave observations during SMEX03," *IEEE Trans. Geosci. Remote Sens.*, vol. 43, no. 11, pp. 2418–2430, Nov. 2005.

[8] T. Markus, D. J. Cavalieri, A. J. Gasiewski, M. Klein, J. A. Maslanik, D. C. Powell, B. B. Stankov, J. C. Stroeve, and M. Sturm, "Microwave signatures of snow on sea ice: Observations," *IEEE Trans. Geosci. Remote Sens.*, vol. 44, no. 11, pp. 3081–3090, Nov. 2006.
[9] I. Corbella, "Calibration of the analog polarimetric scanning radiometer (PSR/A)," NOAA/Environ. Res. Lab., Boulder, CO, p. 59, 1999.
[10] B. B. Stankov, D. Cline, and M. Tedesco, "Empirical SWE retrieval using airborne microwave and *in situ* snow measurements," in *Proc. IEEE IGARSS*, Barcelona, Spain, Jul. 23–28, 2007, pp. 1444–1447.
[11] D. W. Cline, R. Armstrong, R. Davis, K. Elder, and G. Liston, *CLPX-Ground: ISA Snow Depth Transects and Related Measurements*, M. Parsons and M. J. Brodzik, Eds. Boulder, CO: Nat. Snow Ice Data Center, 2003. [Digital media].
[12] D. W. Cline, R. Armstrong, R. Davis, K. Elder, and G. Liston, *CLPX-Ground: ISA Snow Pit Measurements*, M. Parsons and M. J. Brodzik, Eds. Boulder, CO: Nat. Snow Ice Data Center, 2002. updated July, 2004. [Digital media].
[13] D. W. Cline and T. Carrol, *CLPX-Airborne: Airborne Gamma Snow and Soil Moisture Surveys*. Boulder, CO: Nat. Snow Ice Data Center, 2004. [Digital media].
[14] J. McGinley, S. Albers, and P. Stamus, "Local data assimilation and analysis for nowcasting," *Adv. Space Res.*, vol. 12, no. 7, pp. 179–188, Jul. 1992.
[15] A. J. Gasiewski and D. B. Kunkee, "Calibration and applications of polarization correlating radiometers," *IEEE Trans. Microw. Theory Tech.*, vol. 41, no. 5, pp. 767–773, May 1993.
[16] F. T. Ulaby, R. K. Moore, and A. K. Fung, *Microwave Remote Sensing Active and Passive, From Theory to Applications*, vol. 3. Reading, MA: Addison-Wesley, 1988, p. 2162.
[17] A. J. Gasiewski and D. H. Staelin, "Numerical modeling of passive microwave O_2 observations over precipitation," *Radio Sci.*, vol. 25, no. 3, pp. 217–235, May/Jun. 1990.
[18] J. T. Pulliainen, J. Grandell, and M. T. Hallikainen, "HUT snow emission model and its applicability to snow water equivalent retrieval," *IEEE Trans. Geosci. Remote Sens.*, vol. 37, no. 3, pp. 1378–1390, May 1999.
[19] G. S. Poulos, D. A. Wesley, and J. S. Snook, "Causes of simultaneous lee and upwind record snowfall and extraordinary snowfall variation in a Rocky Mountain blizzard," in *Proc. 28th ICAM Annu. Sci. Meeting MAP*, Zadar, Croatia, May 23–27, 2005.
[20] F. Mesinger, G. DiMego, E. Kalnay, K. Mitchell, P. C. Shafran, W. Ebisuzaki, D. Joviæ, J. Woollen, E. Rogers, E. H. Berbery, M. B. Ek, Y. Fan, R. Grumbine, W. Higgins, H. Li, Y. Lin, G. Manikin, D. Parrish, and W. Shi, "North American Regional Reanalysis," *Bull. Amer. Meteorol. Soc.*, vol. 87, no. 3, pp. 343–360, Mar. 2006.
[21] G. S. Poulos, P. Stamus, and J. Snook, *CLPX NCAR Data Analysis and Numerical Modeling*. Boulder, CO: Nat. Snow Ice Data Center, 2007. [Digital media].
[22] R. Bindlish, T. J. Jackson, A. Gasiewski, B. Stankov, M. Klein, M. H. Cosh, I. Mladenova, C. Watts, E. Vivoni, V. Lakshmi, J. Bolten, and T. Keefer, "Aircraft based soil moisture retrievals under mixed vegetation and topographic conditions," *Remote Sens. Environ.*, vol. 112, no. 2, pp. 375–390, Feb. 2008.
[23] E. Schanda, C. Matzler, and K. Kunzi, "Microwave remote sensing of snow covers," *Int. J. Remote Sens.*, vol. 4, no. 1, pp. 149–158, 1983.
[24] C. Matzler, E. Schanda, and W. Good, "Towards the definition of the optimum sensor specifications for microwave sensing of snow," *IEEE Trans. Geosci. Remote Sens.*, vol. GRS-20, no. 1, pp. 57–66, Jan. 1982.
[25] M. T. Hallikainen and P. A. Jolma, "Comparison of algorithms for retrieval of snow water equivalent from nimbus-7 SMMR Data in Finland," *IEEE Trans. Geosci. Remote Sens.*, vol. 30, no. 1, pp. 124–131, Jan. 1992.

Borislava Boba Stankov received the B.S. degree in meteorology from Belgrade University, Belgrade, Yugoslavia, in 1964, and the M.S. degree in atmospheric sciences from the Colorado State University, Fort Collins, in 1970. She completed all requirements for a Ph.D. at the University of Colorado, Boulder, in 1978. In 1998, she defended her thesis at Macquarie University, Sydney, Australia, and received the Ph.D. degree.

From 1964 to 1968, she was a Forecaster with the Yugoslav Weather Bureau. From 1968 to 1978, she was a Graduate Student with the Colorado State University and the University of Colorado. From 1978 to 1985, she was a Scientist with the Boundary Layer Research Division, National Center for Atmospheric Research, Boulder. From 1985 to January 31, 2008, she was a Scientist with the Earth Systems Research Laboratory, National Oceanic and Atmospheric Administration (NOAA), Boulder. Until 1987, her research interests concentrated on boundary-layer (BL) turbulence studies using *in situ* airborne high-frequency sampling instrumentation. She studied BL length scales in convective and stable conditions, and ozone concentration in the BL. Since 1987, her interests focused on the ground-based, space-based, and combined ground- and space-based microwave sounding of the atmosphere. She developed a method for multisensor retrieval of atmospheric properties using both active and passive remote sensor measurements to improve the atmospheric sounding resolution within the BL. Since 2001, she has conducted research using the airborne polarimetric scanning radiometer measurements of the Earth's surface properties. After retiring from the NOAA in January 2008, she joined the Cooperative Institute for Research in Environmental Sciences, University of Colorado.

Dr. Stankov is a member of the Yugoslav and American Meteorological Societies, the American Institute of Aeronautics and Astronautics, and the International Union of Radio Science Commission F.

Donald W. Cline received the B.A., M.A., and Ph.D. degrees in geography from the University of Colorado, Boulder, in 1989, 1992, and 1995, respectively.

He completed postdoctoral positions with the Department of Hydrology and Water Resources, University of Arizona, Tucson; the School for Environmental Science and Management, University of California, Santa Barbara; and the Institute for Arctic and Alpine Research, University of Colorado. Since 1998, he has been with the National Oceanic and Atmospheric Administration, Chanhassen, MN, where he is the Director of the National Operational Hydrologic Remote Sensing Center of the National Weather Service. He has developed and taught courses in surface water hydrology, snow hydrology, geographic information systems, and remote sensing. His scientific and technical interests include hydrologic remote sensing, hydrological modeling, geospatial terrain analysis, and cryospheric science.

Dr. Cline is a member of the American Geophysical Union.

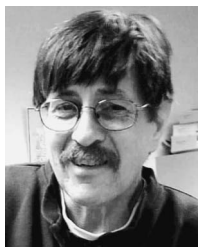

Bob L. Weber received the B.S. and Ph.D. degrees in physics from Ohio State University, Columbus, in 1965 and 1975, respectively.

From 1966 to 1974, he was a Research Physicist with Battelle Memorial Institute, Columbus, OH, where he worked on optical signal processing, holography, nonlinear plasma wave propagation, radio wave propagation and scattering in the ionosphere, nonlinear ocean wave motion, and radio wave scattering from the ocean surface. From 1974 to 2003, he was a Supervisory Physicist with the Earth System Research Laboratory (ESRL), U.S. National Oceanic and Atmospheric Administration (NOAA), Boulder, CO. Starting in 1992, he worked with multiple government agencies and industry to lead the development of the Mobile Profiler System, which is an integrated system of ground-based and satellite-borne remote sensors. He played a critical role in establishing a joint program with the National Weather Service (NWS) and the U.S. Air Force to develop 449-MHz profilers' technology, with the first new radars installed in Alaska and Vandenberg Air Force Base in California. From 2001 to 2003, he served as Deputy Chief of the Microwave Systems Development Branch, Physical Science Division. Since 2003, he has been a Contractor with the ESRL. Since 2006, he has been a Senior Research Associate with the Center for Environmental Technology (CET), Department of Electrical and Computer Engineering, University of Colorado, Boulder. He has worked upon airborne and ground-based microwave radiometric observations of the atmosphere and surface and the assimilation of satellite microwave radiances into numerical weather prediction models since 2003. His research and interests have ranged from ocean remote sensing and electromagnetic scattering from rough surfaces, nonlinear wave theory and turbulence, to remote sensing of the atmosphere using both active radars and passive radiometers.

Dr. Weber conducted experimental and theoretical research from 1974 to 1984 relating to the remote sensing of the ocean, receiving the Gold Medal (the highest civilian award) in 1978 for distinguished achievement, the distinguished authorship award from the U.S. Department of Commerce, and the Special Acts award in 1984.

Albin J. Gasiewski (S'81–M'88–SM'95–F'02) received the B.S. and M.S. degrees in electrical engineering and the B.S. degree in mathematics from Case Western Reserve University, Cleveland, OH, in 1983, and the Ph.D. degree in electrical engineering and computer science from the Massachusetts Institute of Technology, Cambridge, in 1989.

From 1989 to 1997, he was an Associate Professor with School of Electrical and Computer Engineering, Georgia Institute of Technology, Atlanta. From 1997 to 2005, he was with the Environmental Technology Laboratory (ETL), National Oceanic and Atmospheric Administration, Boulder, CO, where he was the Chief of ETL's Microwave Systems Development Division. He is currently a Professor of electrical and computer engineering with the University of Colorado, Boulder, and the Director of the CU Center for Environmental Technology. He has developed and taught courses on electromagnetics, remote sensing, instrumentation, and wave propagation theory. His technical interests include passive and active remote sensing, radiative transfer, antennas and microwave circuits, electronic instrumentation, meteorology, and oceanography.

Prof. Gasiewski was the President of the IEEE Geoscience and Remote Sensing Society (2004–2005) and a Founding Member of the IEEE Committee on Earth Observation. He is a member of the American Meteorological Society, the American Geophysical Union, the International Union of Radio Scientists (URSI), Tau Beta Pi, and Sigma Xi. He served on the U.S. National Research Council's Committee on Radio Frequencies from 1989 to 1995. He was the General Cochair of the IEEE International Geoscience and Remote Sensing Symposium 2006, Denver, CO. He was the recipient of the 2006 Outstanding Service Award from the Geoscience and Remote Sensing Society. He currently serves as the Vice Chair of the United States National Committee/URSI Commission F.

Gary A. Wick received the B.S., M.S., and Ph.D. degrees in aerospace engineering sciences from the University of Colorado, Boulder, in 1988, 1990, and 1995, respectively.

Since 2000, following the completion of a postdoctoral position at the Applied Physics Laboratory, University of Washington, Seattle, and an employment through the Cooperative Institute for Research in Environmental Sciences at the University of Colorado, he has been a Physicist with the Physical Sciences Division, Earth System Research Laboratory, National Oceanic and Atmospheric Administration (NOAA) and its predecessor laboratories. Recently, he has become involved in the new NOAA Unmanned Aircraft Systems project, where he is the Coleader of the Pacific Test bed. His research has focused on the development of physical models and the application of infrared and microwave satellite remote-sensing data to studies in oceanography, meteorology, and air–sea interactions.